Degree Thesis

Stress Concentration Analysis of Materials

Author: Lien Tran

Instructor: Mathew Vihtonen

Degree Programme: Plastics Technology

Date: 29/04/2016

DEGREE THESIS	
Arcada	
Degree Programme:	Plastics Technology
Identification number:	16563
Author:	Lien Tran
Title:	Stress Concentration Analysis of Materials
Supervisor (Arcada):	Mathew Vihtonen
Commissioned by:	Rene Herrmann

Abstract:

This thesis work is to study the stress concentration around a circular hole with different radius in a finite width, tensile loaded plate by the experimental methods including tensile testing and photoelasticity, and computational method performed by COMSOL Multiphysics. Holes with diameter of 1, 2, 3, 4, and 5 mm were drilled in the middle of ASTM D638 standard specimens which were prepared by injection moulding technique. Photoelastic techniques were used to observe the available stresses in free of load condition in a series of two-dimensional models. Polyethylene terephthalate was chosen to study due to its high birefringent index.

The stress concentration factor obtained from computational method is 6% greater than that derived from theoretical method. As the ratio of hole diameter over specimen's width increases from 0 to 0.83, the stress concentration factor decrease from 3 to 2.94 in theoretical method and from 2.71 to 2.16 in computational method. The stress concentration factor is independent from materials made up the element but geometry, notch sensitivity, on the contrary, is material factor which is used to predict the fatigue strength of structural element containing holes. The study shown a result that fatigue strength of material reduces roughly 50% as the diameter of the hole increases by 1 mm in a same width specimen. Experimental fatigue strength shows 30% lower in magnitude compared to theoretical predicted value.

Keywords:	Stress Concentration, Photoelasticity, Birefringence, Polarization, Stress and Strain, Mohr's circle.
Number of pages:	
Language:	English
Date of acceptance:	

CONTENTS

1 INTRODUCTION 11

1.1 Background 11
1.2 Objectives 12

2 LITERATURE REVIEW 13

2.1 Stress and Strain 13
2.1.1 Stress 13
2.1.2 The Stress Tensor 16
2.1.3 Principal Stress: 17
2.1.4 Mohr's Circle 20
2.1.5 Strain 22
2.2 Stress concentrations 22
2.2.1 Stress Concentration around a Hole and Nominal Stresses Definition 23
2.2.2 Stress Concentration as a Two-Dimensional Problem 24
2.2.3 Notch Sensitivity and Fatigue Stress 25
2.3 Photoelasticity 26
2.3.1 Introduction 26
2.3.2 Electromagnetic Wave Representation of Light 27
2.3.3 Refraction 29
2.3.4 Polarization 29
2.3.5 Linear Polarizer and Quarter-wave Plate 33
2.3.6 Stress and Birefringence 34
2.4 Injection Moulding 36
2.4.1 Machinery 36
2.4.2 Mould 37
2.4.3 Injection Moulding Parameters 38

3 METHOD 40

3.1 Material 40
3.2 Samples Preparing by Injection Moulded 40
3.3 Tensile Testing 40
3.4 Comsol Model 41
3.5 Photoelasticity Setup 43

4 RESULTS 45

4.1 Mathematical Analysis 45
4.2 Tensile Testing 48
4.3 COMSOL Simulation 48

4.4 Photoelastic Observation 51

5 DISCUSSION 53

5.1 Stress Concentration Factor and Maximum Stresses 53

5.2 Fatigue Strength Predication 53

6 CONCLUSION 55

REFERENCES 56

APPENDIX I 58

APPENDIX II 59

APPENDIX III 60

Figures

Figure 1: Internal forces in a solid body under a self-equilibrating system of forces (Silva, 2006). 14
Figure 2: Stress in an infinitesimal surface (Silva, 2006). 15
Figure 3: Positive normal and shearing stresses (Silva, 2006). 16
Figure 4: Infinitesimal prism used in the two-dimensional analysis of the stress state. (Silva, 2006) 20
Figure 5: Mohr's representation for the two-dimensional stress state. (Silva, 2006) and (Javidinejad, 2015) 21
Figure 6: Mohr's representation of the stress state in the three-dimensional case. (Silva, 2006) 21
Figure 7: Tension bar with a hole. (Walter and Deborah , 2008) 24
Figure 8: The electric and magnetic fields of a linearly polarized wave (Chen, 2000). 29
Figure 9: Propagation of the transverse optical field (Goldstein, 2011) 31
Figure 10: Motion of the plane or linear polarized light vectors (Chen, 2000). 32
Figure 11: Motion of the circular polarized light vectors (Chen, 2000). 32
Figure 12: State of polarization of a light wave after passing through a $\lambda/4$ plate (whose fast axis is indicated by the double arrow) for different azimuths of the incident plane-polarized beam. (Bannett, 1995) 34
Figure 13: Specimen dimension 41
Figure 14: Tensile testing specimens 41
Figure 15: Arrangement of the optical elements in a plane polariscope. (Chen, 2000) 43
Figure 16: Transmitting and absorbing characteristic of a plane polarizer and in a stressed photoelastic model. (Chen, 2000) 44
Figure 17: Transmission of the components of the light vectors through the analyzer. (Chen, 2000) 44
Figure 18: Stresses in an inclined section (Silva, 2006). 45
Figure 19: Mohr's Circle for uniaxial tension. 47
Figure 20: Tensile strength value by theory and practice. 48
Figure 21: Mesh results of non-hole profile and profiles with hole of 1, 2, 3, 4, 5mm in diameter. 49

Figure 22: Computational results for profiles with hole of 1, 2, 3, 4, and 5 mm in diameter. 50
Figure 23: Photoelasticity observation for 1, 2, 3, 4, and 5 mm diameter-hole-samples in un-loaded state. 52

Tables

Table 1: PET's input parameters. 42
Table 2: Load description 42
Table 3: Mesh's statistics and size. 42
Table 4: Stress concentration factor for various d/H ratio. 47

Notation

B	Magnetic field.
c	Speed of light.
c_a	The speed of light in the surrounding medium.
c_s	The speed of light in the substance.
c_1	Direct stress-optic coefficient.
c_2	Transverse stress optic coefficient.
C	Stress-optic coefficient.
d	Hole diameter.
dF	Infinitesimal force.
$d\Omega$	Infinitesimal area.
E	Electric field.
F_σ	Material stress fringe value.
k	Wave vector.
K_c	Computational stress concentration factor.
K_t	Theoretical stress concentration factor.
K_e	Effective stress concentration factor.
K_f	The estimated fatigue notch factor for normal stress.
K_{fs}	The estimated fatigue notch factor for shear stress.
K_{tg}	Stress concentration factor based on gross sectional area.
K_{tn}	Stress concentration factor based on net cross sectional area.
H	The width of specimen.
h	The thickness of specimen.
n	Refractive index in the unstressed state.
n_s	Index of refraction of substance.
n_1, n_2	Refractive indices for vibrations corresponding to these two directions.
N	Photoelasticity fringe order.
q	The notch sensitivity of materials.
T	Stress defined by load per area.
t	Material thickness.
$\boldsymbol{u}$	Unit vector.
ϵ_0	Electric constant.

μ_0	Magnetic constant.
ϵ	Permittivity of material.
μ	Permeability of material.
φ	An arbitrary phase term.
δ	Phase difference.
$\vec{n}$	Unit vector.
σ	Normal stress.
σ_{nom}	Nominal stress.
τ	Shearing stress.
τ_{nom}	Nominal shearing stress.
ν	Poisson's ratio.

FOREWORD

I wish to express my sincere appreciations to Mr. Mathew Vihtonen and Mr. Rene Herrmann for their excellent supervision throughout this research. Their encouragement and technical guidance has been invaluable. I am particularly appreciative of the valued advice of Mr. Herrmann who has been most supportive throughout this study. I am also grateful for the support of the technical staff Mr. Erland Nyroth in sample manufacturing.

I would like to extend my appreciation to all the teachers and staff for their guidance and inspiration during my three years studying at Arcada University of Applied Sciences.

Finally, I would like to thank my family and friends for their continued support over the last few years, particularly during the completion of this thesis. Special thanks also to Tung for his unlimited encouragement, help and patience especially over the writing up months.

1 INTRODUCTION

1.1 Background

In engineering, stress analysis has been regarded as an extremely important process with the purpose of determining and improving mechanical strength of structures and machines. The present of discontinuities in the members such as holes or notches has a consequence of chances in stress distribution. Near those areas, the magnitudes of stress reach much higher than those of the average stress over the section, especially when fatigue conditions are involved. The study of stress concentration provides fatigue data needed for evaluation of the interaction of machined steps and fastener holes.

The familiar methods of stress analysis consist of experimental stress analysis which is based on experimental means, and computational methods, primarily the finite element method. The experimental stress analysis is performed by applying static or dynamic loads to a test specimen or structure then defining the resulting stresses by appropriate equipment. There are two testing methods which are destructive and non-destructive. Whereas, in computational methods, in this work, finite element method is utilized, which is a numerical technique based on mathematics. This technique provides approximate solutions to boundary value problems for partial differential equations by subdividing a large problem into smaller, simpler finite elements. (Reddy, 2006)

Another method of stress study is photoelasticity which based on property of crystal called double refraction or birefringence. The concept of birefringence on optical materials was first observed by Sir David Brewster in 1816, which described a phenomenon when a ray of light is incident on certain crystals, it fragments into two components transmitting through material in dissimilar directions. (James F. Doyle and James W. Phillips, 1989) This characteristic of light formerly is applied in photoelasticity or optical stress study. Under stress, an optical material produces interference bands acknowledged as isochromatics or stress fringes when it is observed in a polarized light field. In the plane perpendicular to the incident light beam, each stress fringe denotes a locus of point which is the same maximum shearing stress. Colour changing from dark to bright then to dark

represents an optical cycle. The fringe order starts at zero at initial dark fringe, one at second fringe, and two at third fringe, etc. The colour bands form a contour like pattern across the object due to the irregularity in geometry of the material. Narrowly spaced bands indicates high stress gradients region, while wide spaced bands indicates low stress gradients region.

1.2 Objectives

The research is conducted aiming to investigate the stress concentration factor for specimens with different radius. Therefore, studying the stress concentration factor can be performed for specimens with different radius of holes cut at the middle part of the specimens. In this work, the objectives consist of:

- Studying of stress concentration factor around different radius of holes by theoretical researching method.
- Simulating the stress behaviour of those samples by computational method and comparing those results with those obtained from calculation.
- Comparing the tensile strength obtained from theoretical and tensile testing result.
- Observing the available stress of samples under free-of-load condition by photoelastic method.

2 LITERATURE REVIEW

2.1 Stress and Strain

The mechanical behaviour of a component used in engineering is determined by the variation of load resultants distributing throughout its body and the characteristic parameters of material makeup of the component. A component may have a complicated geometry with various dimensions. However, due to the fact that the material parameters of a component are independent from its geometry and dimension their mechanical behaviour can be determined in experiments using standardised specimens. The varying condition within a component can be described by the load and deformation measures specified for small volume elements, in which a continuum mechanical approach is applied. In specific, the matter is considered to be distributed continuously, therefore, all variables are continuous. (Rösler et al., 2007)

2.1.1 Stress

Stress is defined as a distribution of force on an external or internal surface body. Consider a solid body under a system of self-equilibrating forces, a state of stress at an arbitrary point P in a body is determined by exposing an infinitesimal surface dΩ or facet containing the point P. The surface is a planar slide with an arbitrary orientation throughout the body and intersects the point P. The equilibrium condition occurs when the internal forces and the external forces acting on the body have the same magnitude and are in opposite directions. By considering the area dΩ, a homogeneous distribution of the internal force in this area is considered. Therefore, the total stress or force per unit area is determined by dividing the infinitesimal force dF by the infinitesimal area dΩ (Javidinejad, 2015) :

$$T = \frac{dF}{d\Omega} \tag{2–1}$$

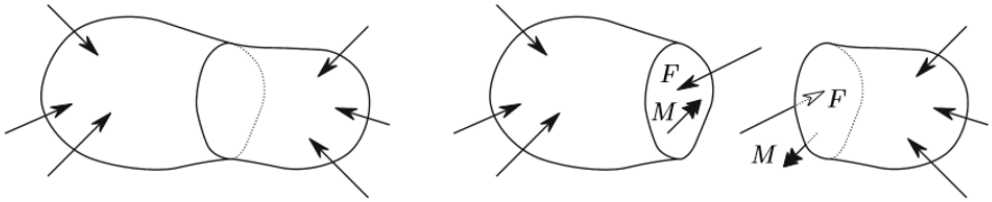

Figure 1*: Internal forces in a solid body under a self-equilibrating system of forces (Silva, 2006).*

To demonstrate the external and internal force distributing across the exposed surface containing the point P of interest, the Cartesian coordinate is used with the y and z axes perpendicular to x axis, and tangential to the surface. For the simple case, the orientation of the infinitesimal surface dΩ can be set as a vector $\vec{n}$ which is perpendicular to the surface at point P and have a direction pointing out from the part of the body considered. The vector $\vec{n}$ is the semi-normal of the surface and acts as a unit vector ($l^2 + m^2 + n^2 = 1$) consisting of three components as the cosines of the angles between the vector and the coordinate axis (Silva, 2006):

$$\begin{cases} n_x = cos(n,x) = l \\ n_y = cos(n,y) = m \\ n_z = cos(n,z) = n \end{cases} \quad (2\text{–}2)$$

The stress acting on the infinitesimal surface are decomposed into two components:

- Normal component σ = T cosα, which is parallel to one of the coordinate axes,
- And a tangential or shearing component τ = T sinα, which is decomposed in the directions of the other two coordinate axes.

  Where α is the angle between the vector $\vec{n}$ and the total stress vector $\overrightarrow{T}$. (Silva, 2006).

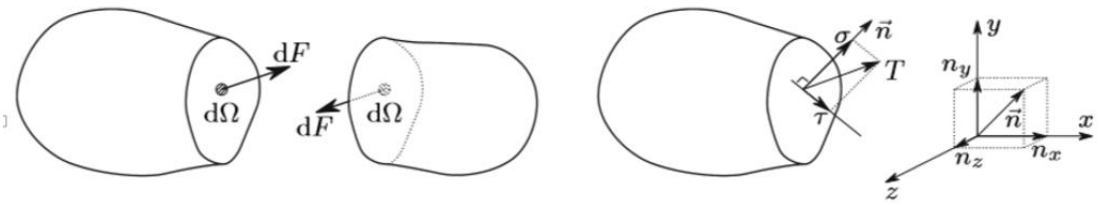

***Figure 2**: Stress in an infinitesimal surface (Silva, 2006).*

The state of stress acting around the chosen point in the body is represented by "cutting out" a cubit volume element of material with the cutting plane preferentially chosen parallel to the coordinate axes. On each face of the element experiences three components of the state of stress acting as presented in ***Figure 3***. (Silva, 2006) . The force distribution at the point P consists of components in the normal and tangential directions which are caused by tensile or compressive and shear stresses acting on the body. As dΩ approaches zero, so do the force and its components, however, the stress or the intensity of the internal force acting on a specific plane passing through a point will approach a finite limit. (Silva, 2006)

$$\sigma = \lim_{d\Omega \to 0} \frac{dF}{d\Omega} \qquad (2\text{–}3)$$

The relative orientation of the force and the area distinguish the stresses, where normal stress is defined by the force F perpendicular to the surface area, and shear stress by the force F parallel to the area. (Rösler et al., 2007).

Based on the Von-Karman convention, the stresses parallel to the axes x, y, and z are denoted as $\sigma_{x,}\ \sigma_{y},$ and σ_{z} respectively. The shearing stresses are represented as τ_{ij} with the first index expresses the direction of the semi- normal of the infinitesimal surface and the second one the direction of the shearing stress vector. The magnitude of the force components is positive if they have the same direction as the coordinate axes to which they are parallel. (Silva, 2006)

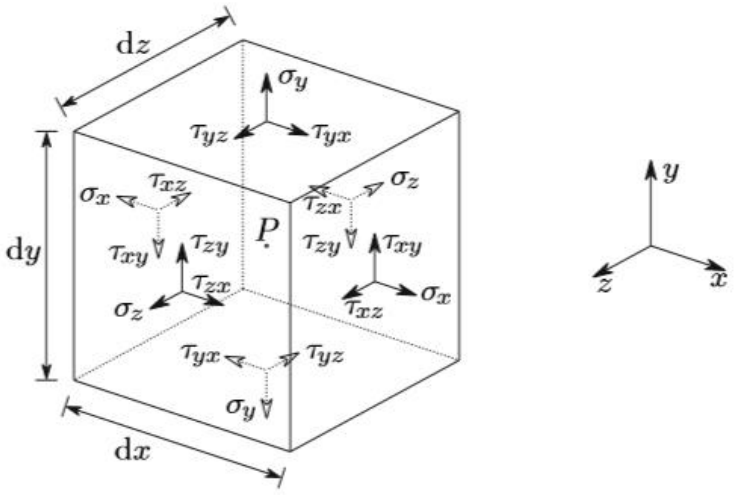

***Figure 3**: Positive normal and shearing stresses (Silva, 2006).*

2.1.2 The Stress Tensor

The nine stress components relating to the Cartesian coordinate axes can be represented in array form known as the stress tensor (Silva, 2006):

$$[\sigma] = \begin{bmatrix} \sigma_x & \tau_{xy} & \tau_{xz} \\ \tau_{yx} & \sigma_y & \tau_{yz} \\ \tau_{zx} & \tau_{zy} & \sigma_z \end{bmatrix} \tag{2–4}$$

The stresses acting on an inclined infinitesimal surface whose components of its orientation vector is not parallel to any of the coordinate axes may be obtained by (Silva, 2006):

$$\begin{bmatrix} T_x \\ T_y \\ T_y \end{bmatrix} = \begin{bmatrix} \sigma_x & \tau_{xy} & \tau_{xz} \\ \tau_{yx} & \sigma_y & \tau_{yz} \\ \tau_{zx} & \tau_{zy} & \sigma_z \end{bmatrix} \begin{Bmatrix} l \\ m \\ n \end{Bmatrix} \tag{2–5}$$

Where T_x, T_y, T_z are the components in the reference of the stress vector acting on the surface of interest, and l, m, and n are the direction cosines of its semi-normal.

According to the reciprocity of the shearing stresses, only six of its nine components are independent (Javidinejad, 2015):

$$\tau_{xy} = \tau_{yx}, \tau_{xz} = \tau_{zx}, and\ \tau_{yz} = \tau_{zy} \tag{2–6}$$

Those six compenents are adequate to determine the state of stress around a point. The normal stress component, therefore, is the projection of vector T in the direction of the semi-normal to the surface (Javidinejad, 2015):

$$\sigma = lT_x + mT_y + nT_z$$

$$= l^2\sigma_x + m^2\sigma_y + n^2\sigma_z + 2lm\tau_{xy} + 2ln\tau_{xz} + 2mn\tau_{yz} \quad (2–7)$$

The shear stress components in the reference direction are obtained by (Silva, 2006):

$$\begin{cases} \tau_x = T_x - l\sigma \\ \tau_y = T_y - m\sigma \\ \tau_z = T_z - n\sigma \end{cases} \quad (2–8)$$

The relationship of the normal stress and shear stress can be obtained by the mean of Pythagoras' theorem: $\tau^2 = T^2 - \sigma^2$ (Silva, 2006).

2.1.3 Principal Stress:

The stress tensor [σ] can be considered as a linear operator when the stress vector has the same direction as the normal to the surface of interest. In this case, the shearing stress disappears, the stresses in those principal surfaces are defined as the principal stresses and their normal vectors are the principal directions of the stress state. (Silva, 2006)

In the principal facet, the stress acting on it consists of only normal component σ:

$$\begin{cases} T_x = l\sigma \\ T_y = m\sigma \\ T_z = n\sigma \end{cases} \quad (2–9)$$

Therefore,

$$\begin{bmatrix} \sigma_x - \sigma & \tau_{xy} & \tau_{xz} \\ \tau_{yx} & \sigma_y - \sigma & \tau_{yz} \\ \tau_{zx} & \tau_{zy} & \sigma_z - \sigma \end{bmatrix} \begin{Bmatrix} l \\ m \\ n \end{Bmatrix} = \begin{Bmatrix} 0 \\ 0 \\ 0 \end{Bmatrix} \quad (2–10)$$

$$[C]$$

The matrix implies a trivial solution of $l = m = n = 0$, and non-zero solutions only if there is a linear dependency between the equations, in the other words, if the determinant of

the system matrix, [C], vanishes. However, the direction cosines *l*, *m*, *n* are the components of a unit vector, hence, they cannot be zero simultaneously. Thus the principal stresses are the roots of the below expression:

$$\begin{vmatrix} \sigma_x - \sigma & \tau_{xy} & \tau_{xz} \\ \tau_{yx} & \sigma_y - \sigma & \tau_{yz} \\ \tau_{zx} & \tau_{zy} & \sigma_z - \sigma \end{vmatrix} = -\sigma^3 + I_1\sigma^2 + I_2\sigma + I_3 = 0 \quad \textbf{[Characteristic Equation]} \tag{2–11}$$

Where:

$$I_1 = \sigma_x + \sigma_y + \sigma_z \tag{2–12}$$

$$I_2 = \begin{vmatrix} \sigma_x & \tau_{xy} \\ \tau_{xy} & \sigma_y \end{vmatrix} + \begin{vmatrix} \sigma_x & \tau_{xz} \\ \tau_{xz} & \sigma_z \end{vmatrix} + \begin{vmatrix} \sigma_y & \tau_{yz} \\ \tau_{yz} & \sigma_z \end{vmatrix} \tag{2–13}$$

$$=\sigma_x\sigma_y + \sigma_x\sigma_z + \sigma_y\sigma_z - {\tau_{xy}}^2 - {\tau_{xz}}^2 - {\tau_{yz}}^2$$

$$I_3 = \begin{vmatrix} \sigma_x & \tau_{xy} & \tau_{xz} \\ \tau_{yx} & \sigma_y & \tau_{yz} \\ \tau_{zx} & \tau_{zy} & \sigma_z \end{vmatrix} = \sigma_x\sigma_y\sigma_z + 2\tau_{xy}\tau_{yz}\tau_{zx} - \sigma_x{\tau_{yz}}^2 - \sigma_y{\tau_{xz}}^2 - \sigma_z{\tau_{xy}}^2 \tag{2–14}$$

Usually the principal stresses are symbolized by $\sigma_1,\ \sigma_2, \text{and}\ \sigma_3$ where $\sigma_1 > \sigma_2 > \sigma_3$. They are independent from the reference system chosen and the reference system used to describe the stress tensor. (Silva, 2006).

It always exists three roots derived from the Characteristic Equation. In one possibility, the results can be obtained as: $\begin{cases} \sigma_1 = \sigma_2 = \sigma_x = \sigma_y \\ \sigma_3 = \sigma_z \end{cases}$. This implies that all the normal stresses of the plane, which are perpendicular to the principal direction corresponding to the third root, are principal stresses and the stress state is symmetric in respect to z axis.

In case that the Characteristic Equation has an equal triple root ($\sigma_1 = \sigma_2 = \sigma_3 = \sigma_x = \sigma_y = \sigma_z$) , the shear stresses vanish in all facets ($\tau_{xy} = \tau_{yz} = \tau_{xz} = 0$) and the normal stress has the same value in every facet entitled as isotropic stress state. (Silva, 2006)

The last possible roots are three different principal stresses when the corresponding principal directions are perpendicular to each other.

On an inclined facet or in two-dimension x and y, the angle θ, which is the orientation of the third face, is defined as an angle between its semi-normal and axis x. Then the equilibrium condition of the forces acting in direction θ yields (Silva, 2006):

$$\sigma_\theta = \frac{\sigma_x+\sigma_y}{2} + \frac{\sigma_x-\sigma_y}{2} cos2\theta + \tau_{xy} sin2\theta \quad (2–15)$$

$$\tau_\theta = -\frac{\sigma_x-\sigma_y}{2} sin2\theta + \tau_{xy} cos2\theta \quad (2–16)$$

The principal stresses, therefore, are defined by (Javidinejad, 2015):

$$\frac{\partial\sigma_\theta}{\partial\sigma} = -(\sigma_x - \sigma_y) sin2\theta + 2\tau_{xy} cos2\theta = 0 \quad (2–17)$$

$$\rightarrow tan2\theta = \frac{2\tau_{xy}}{\sigma_x-\sigma_y} \rightarrow \theta = \frac{1}{2}\tan^{-1}\left(\frac{2\tau_{xy}}{\sigma_x-\sigma_y}\right) \quad (2–18)$$

$$\sigma_{1,2} = \frac{\sigma_x+\sigma_y}{2} \pm \sqrt{\left(\frac{\sigma_x-\sigma_y}{2}\right)^2 + {\tau_{xy}}^2} \quad (2–19)$$

Likewise, for the maximum shear (Javidinejad, 2015):

$$\frac{\partial\sigma_\tau}{\partial\sigma} = -2\frac{(\sigma_x-\sigma_y)}{2} cos2\theta - 2\tau_{xy} sin2\theta = 0 \quad (2–20)$$

$$\rightarrow tan2\theta = -\frac{\sigma_x-\sigma_y}{2\tau_{xy}} \rightarrow \theta = \frac{1}{2} tan^{-1}\left(-\frac{\sigma_x-\sigma_y}{2\tau_{xy}}\right) \quad (2–21)$$

In a two-dimensional stress state, there are always two orthogonal directions defining facets where the shearing stress has a zero value and where the normal stress takes its minimum and maximum values (usually denoted as σ_1 and σ_2 respectively). This is because θ can have 2 values: $\theta_1$and $\theta_2 = \theta_1 + \frac{\pi}{2}$ which correspond to maximum and minimum of σ_θ.

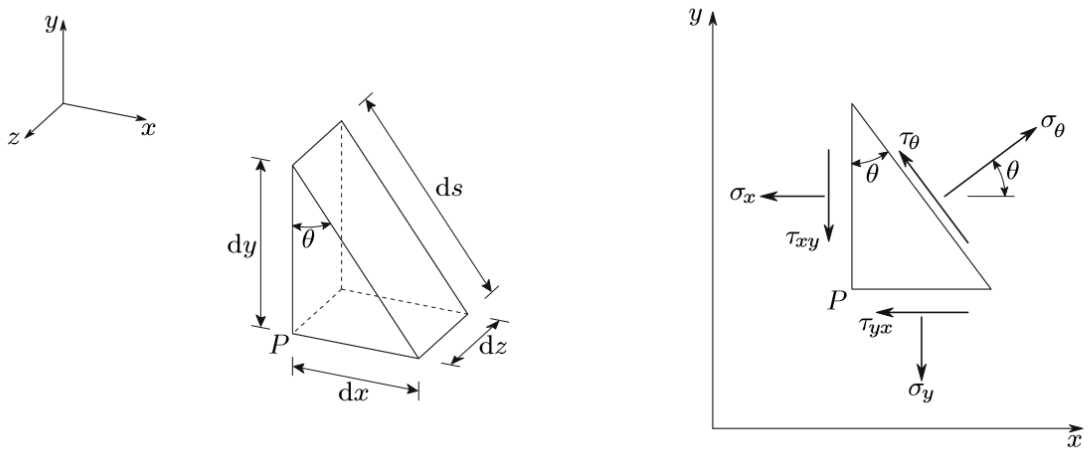

***Figure 4**: Infinitesimal prism used in the two-dimensional analysis of the stress state. (Silva, 2006)*

2.1.4 Mohr's Circle

Mohr's Circle is used to represent the whole stress state or stress tensor graphically, which was developed by Otto Mohr in the end of 19th century. The stress vector in every facet whose orientation defined by angle α can be represented by a single point in the circle. The horizontal direction (or axis of abscissas) represents the normal stresses, and the vertical one (axis of ordinates) represents the shearing stress with sign convention, where a positive stress corresponds to the y-direction in a referential system, which is obtained by a rotation θ in the direct direction (counter clockwise). Accordingly, a positive shearing stress in the inclined facet corresponds to a rotation, in the direct direction, around point P. (Silva, 2006)

Figure 5 shows a circle with radius of $\frac{\sigma_1-\sigma_2}{2}$, the centre is a point of $\frac{\sigma_1+\sigma_2}{2}$ in the axis of abscissa and zero ordinate. The facet with a semi-normal, whose orientation is defined by an angle α (with θ = α) measured from the principal direction 1 is represented by point A in the figure. The angle is positive in the counter-clockwise direction. The extreme value of the shearing stress ($\tau_\theta = \frac{\sigma_x-\sigma_y}{2}$) is the radius of the Mohr's circle which occurs in facet having an orientation of 45^0 in relationship to the principle direction. Whereas, the maximum value of normal stress occurs at the facets having zero value of shearing stress. (Silva, 2006)

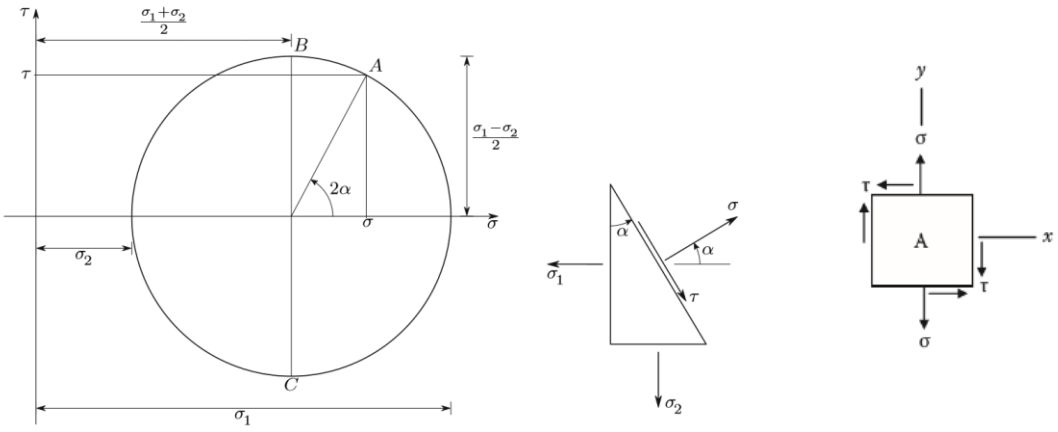

***Figure 5**: Mohr's representation for the two-dimensional stress state. (Silva, 2006) and (Javidinejad, 2015)*

Figure 6 illustrates the representation of the whole state of stress in 3 dimensions in the Mohr's plane. The plane is constructed by three circles defined by the three pairs of principal stresses. The shaded area represents the facets whose directions are not parallel to any of the principal directions. This is based on the solution of the system of equations (Silva, 2006):

$$\begin{cases} l^2 + m^2 + n^2 = 1 \\ l^2\sigma_1 + m^2\sigma_2 + n^2\sigma_3 = \sigma \\ l^2{\sigma_1}^2 + m^2{\sigma_2}^2 + n^2{\sigma_3}^2 = \sigma^2 + \tau^2 \end{cases} \leftrightarrow \begin{bmatrix} 1 & 1 & 1 \\ \sigma_1 & \sigma_2 & \sigma_3 \\ {\sigma_1}^2 & {\sigma_2}^2 & {\sigma_3}^2 \end{bmatrix} \begin{Bmatrix} l^2 \\ m^2 \\ n^2 \end{Bmatrix} = \begin{Bmatrix} 1 \\ \sigma \\ \sigma^2 + \tau^2 \end{Bmatrix} \tag{2–22}$$

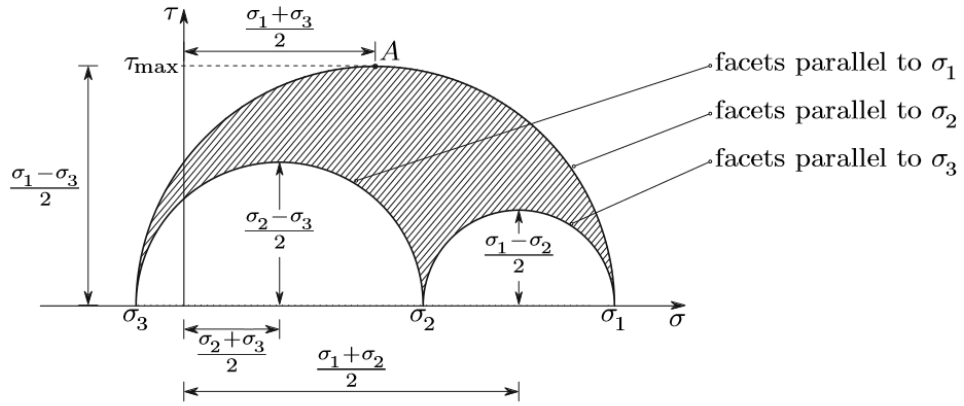

***Figure 6**: Mohr's representation of the stress state in the three-dimensional case. (Silva, 2006)*

2.1.5 Strain

As the internal or external forces acting on a body, the material points inside, in result, suffer a displacement which is a consequence of deformation. The external forces are not essentially causes of a rigid body motion or a deformation but the internal forces distributing inside the body unless the displacement coexists with accelerations. Temperature variation or similar phenomena is also a possible cause of deformation. Strain, therefore, is defined as the deformation per length in any direction. Similar to stress, strain tensor is defined by exactly the same mathematical characteristics as the stress tensor under the validity of the continuum hypothesis. (Silva, 2006)

The deformation caused in a body principally varies from one point to another or in other words, non-homogeneous since it causes various rotations and elongations in the different line segments. In general, it results in the transformation of initially simple geometrical shapes into complex shapes. In order to define the deformation inside a body, the method of deformation analysis of an infinitesimal neighbourhood of a point is applied.

2.2 Stress concentrations

In structural members, there usually exists sudden changes of the cross-section such as shoulders, grooves, holes, keyways, threads, and so forth, which cause the material discontinuous in a bar since the cross-sections do not remain plane. As a consequence, stress distribution in the object does not remain uniform, which means that the maximum stress is larger than the mean value obtained by the theory of prismatic members. The location of high stress is acknowledged as stress concentration measured by the stress concentration factor K. Stress concentration is also referred as a stress raiser or stress riser, a local stress increase in the intensity of a stress field due to discontinuity (Whitley, Fall 2013). The K factor is defined as the ratio of the peak stress in the body to some other preference stresses (Walter and Deborah , 2008):

$$K_t = \frac{\sigma_{max}}{\sigma_{nom}} \tag{2–23}$$

$$K_{ts} = \frac{\tau_{max}}{\tau_{nom}} \tag{2–24}$$

In which, σ_{nom}, τ_{nom} are the nominal stresses or reference normal and shear stresses. The stress concentration factor with subscription *t* in this equation is a theoretical factor which is defined by theory of elasticity or computational calculations, or derived from a laboratory stress analysis experiment such as photoelasticity, or strain gage tests from factors obtained through mechanical damage tests. In the plastic range, it is required to consider separate stress and strain concentration factors depending on the shape of stress strain curve and stress and strain level. (Whitley, Fall 2013)

The theory of elasticity is based on the assumption that the material must be isotropic or homogeneous. (Whitley, Fall 2013) However, materials used in reality are usually non-homogenous and even have defects, therefore, more data is required to have an accuracy result of stress concentration factors.

2.2.1 Stress Concentration around a Hole and Nominal Stresses Definition

The stress concentration factor is determined by a proper stress reference. The stress reference is defined by the applied force over the gross-sectional area (Walter and Deborah , 2008):

$$\sigma_{nom} = \frac{P}{Hh} \tag{2–25}$$

The nominal stress can be defined by the net cross-sectional area which is formed by removing the circular hole from the cross section:

$$\sigma_n = \frac{P}{(H-d)h} \tag{2–26}$$

The stress factor determined for a two-dimension element with a single hole becomes:

$$K_{tn} = \frac{\sigma_{max}}{\sigma_{nom}} = \frac{\sigma_{max}}{\sigma_n} = \frac{\sigma_{max}(H-d)h}{P} = K_{tg}\frac{H-d}{H} \tag{2–27}$$

Where σ_{nom}, σ_n: nominal stress [MPa]

K_{tg}: stress concentration factor based on gross sectional area

K_{tn}: stress concentration factor based on net cross sectional area

H: the width of specimen [mm]

h: specimen thickness [mm]

d: hole diameter [mm].

The stress concentration factor obtained in this section can take into account the two effects of increased stress due to loss of section and increased stress due to geometry (Walter and Deborah , 2008). Apart from difference in nominal stresses, K_{tg} and K_{tn} distinguish each other by the ratio of hole diameter and the width of the specimen d/H. As the hole becomes larger, the element becomes narrower, the ratio d/H growths from 0 to 1, K_{tg} growths from 1 to ∞, notwithstanding K_{tn} drops from 3 to 2 (**See Appendix I**).

As shown in ***Figure 7***, the maximum stresses occur at point A of the specimen.

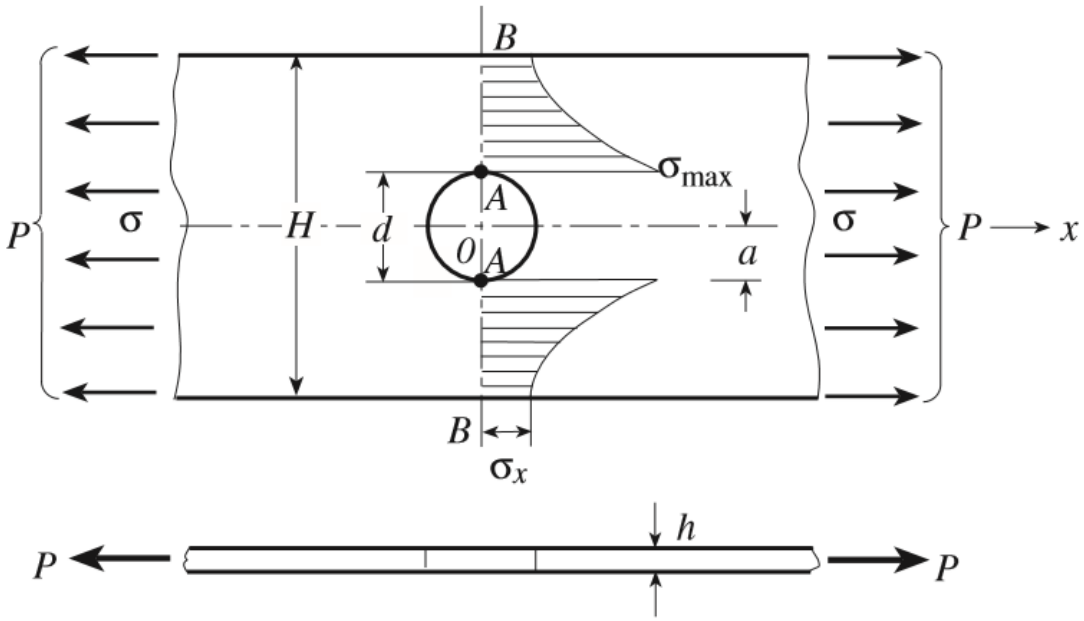

Figure 7*: Tension bar with a hole. (Walter and Deborah , 2008)*

2.2.2 Stress Concentration as a Two-Dimensional Problem

Two dimensional problem is to deal with a thin element which lies in the x, y plan with the applied forces is in the x, y plane at the boundary. The stress components σ_z, τ_{xz}, and τ_{yz} are assumed to be equal to zero and the stress components $\sigma_x, \sigma_y,$ and τ_{xy} are functions of x and y only. Therefore, the state of stress is a plane stress (Walter and Deborah , 2008):

$$\frac{\partial \sigma_x}{\partial x} + \frac{\partial \tau_{xy}}{\partial x} + \bar{p}_{Vx} = 0 \qquad (2\text{–}28)$$

$$\frac{\partial \tau_{xy}}{\partial x} + \frac{\partial \sigma_y}{\partial y} + \bar{p}_{Vy} = 0 \qquad (2\text{–}29)$$

$$\left(\frac{\partial^2}{\partial x^2} + \frac{\partial^2}{\partial y^2}\right)(\sigma_x + \sigma_y) = -f(v)\left(\frac{\partial \bar{p}_{Vx}}{\partial x} + \frac{\partial \bar{p}_{Vy}}{\partial y}\right) \qquad (2\text{–}30)$$

Where $\bar{p}_{Vx}$, $\bar{p}_{Vx}$: components of applied body forces per unit volume in x, y direction

$f(\nu)$: function of Poisson's ratio

$$f(\nu) = \begin{cases} 1+\nu & \text{for plane stress} \\ \frac{1}{1-\nu} & \text{for plane strain} \end{cases} . \quad (2\text{–}31)$$

The surface conditions are: $\begin{cases} p_x = l\sigma_x + m\tau_{xy} \\ p_y = l\tau_{xy} + m\sigma_y \end{cases}$, where p_x, p_y are the components of the surface force per unit area at the boundary in the x, y direction, and l, m are the direction cosines of the normal to the boundary. The constant body forces make $\frac{\partial \bar{p}_{Vx}}{\partial x} = \frac{\partial \bar{p}_{Vy}}{\partial y} = 0$, the stresses distribution for two-dimensional problems with constant body forces are:

$$\left(\frac{\partial^2}{\partial x^2} + \frac{\partial^2}{\partial y^2}\right)(\sigma_x + \sigma_y) = 0 \quad (2\text{–}32)$$

The plane problem with constant body forces has the stress distribution as a function of the body shape and loadings acting on the boundary and not of the material. (Walter and Deborah , 2008)

2.2.3 Notch Sensitivity and Fatigue Stress

In a realistic model, as applied loads reach a certain level, plastic deformations happen. The actual strength of structural members, therefore, is derived from the effective stress concentration factor loads (K_e) instead of theoretical stress concentration factors. The effective stress concentration factor is defined as the factor of stress concentration at rupture or the notch rupture strength ratio. Different from theoretical stress concentration factor (K_t) which depend on element's geometry and applied force condition, the effective stress concentration factor depends on not only of geometry but also of material properties. The relationship between K_e and K_t is (Walter and Deborah , 2008):

$$K_e = q(K_t - 1) + 1 \quad (2\text{–}33)$$

$$K_{es} = q(K_{ts} - 1) + 1 \quad (2\text{–}34)$$

Or $$q = \frac{K_e - 1}{K_t - 1} = \frac{K_{es} - 1}{K_{ts} - 1} \quad (2\text{–}35)$$

Where q: the notch sensitivity of materials (0 < q <1).

The concepts of the effective stress concentration factor and notch sensitivity have a primary influence on fatigue strength of materials predication. The effective stress concentration factor (K_e) is replaced by fatigue notch factor (K_f) for fatigue loading, which is defined as (Walter and Deborah , 2008):

$$K_f = \frac{\text{fatigue limit of unnotched specimen (axial or bending)}}{\text{fatigue limit of notched specimen (axial or bending)}} = \frac{\sigma_f}{\sigma_{nf}} \quad (2\text{–}36)$$

$$K_{fs} = \frac{\text{fatigue limit of unnotched specimen (shear stress)}}{\text{fatigue limit of notched specimen (shear stress)}} = \frac{\tau_f}{\tau_{nf}} \quad (2\text{–}37)$$

The notch sensitivities for fatigue become (Walter and Deborah , 2008):

$$K_f = q(K_t - 1) + 1 \quad (2\text{–}38)$$

$$K_{fs} = q(K_{ts} - 1) + 1 \quad (2\text{–}39)$$

Or $$q = \frac{K_f - 1}{K_t - 1} = \frac{K_{fs} - 1}{K_{ts} - 1} \quad (2\text{–}40)$$

where K_f: the estimated fatigue notch factor for normal stress

K_{fs}: the estimated fatigue notch factor for shear stress.

2.3 Photoelasticity

2.3.1 Introduction

Photoelasticity is an experimental method which is used to determine the stress distribution in a material. The photoelastic phenomenon was first introduced by David Brewster, a Scottish Physicist in 1816 and was developed by E.G.Coker and L.N.G Filon of University of London at the early of the twentieth century. Photoelasticity method provides an important tool for determining the critical stress points in materials that have complicated geometry, complicated loading condition, or both, when the mathematical methods become cumbersome or impossible. The method of photoelasticity is relatively straightforward by offering fairly accurate pictures of stress distribution in both planes and abrupt discontinuities in a member, which is valuable to determine the critical stress points in a part and stress concentration factors in irregular geometries. (Anon., 2009-2016)

The name Photoelasticy is derived from “photo” which denotes the use of light rays and optical properties, while “elasticity” describes the study of stresses and deformation in

elastic members. This method takes advantage of birefringent property which is exhibited by certain optical materials. (James F. Doyle and James W. Phillips, 1989)

2.3.2 Electromagnetic Wave Representation of Light

The nature of light is defined as a transverse, ultra-high frequency electromagnetic wave. The electromagnetism is unified by electricity and magnetism and is described by Maxwell's equations. These equations show that a magnetic field varying with time acts as a source of electric field (**E**) and that an electric field varying with time acts as a source of magnetic field (**B**). These electric field and magnetics fields sustain each other forming an electromagnetic wave that propagate through space without a need of material medium. (Young and Freedman, 2016):

$$\nabla \cdot \mathbf{E} = -\frac{\nabla \cdot \mathbf{P}}{\epsilon_0}$$
$$\nabla \cdot \mathbf{B} = 0$$
$$\nabla \times \mathbf{E} = -\frac{\partial \mathbf{B}}{\partial t}$$
$$\nabla \times \frac{\mathbf{B}}{\mu_0} = \epsilon_0 \frac{\partial \mathbf{E}}{\partial t} + \frac{\partial \mathbf{P}}{\partial t} + \mathbf{J}_{\text{free}}$$

These equations describe the electric and magnetic fields in vacuum. The electric constant ϵ_0 and magnetic constant μ_0 are replaced by permittivity ϵ and permeability μ if there is an exhibition of a material. The value of $1/\sqrt{\epsilon_0 \mu_0}$ gives the correct speed of light c = 299,792,458 m/s. Electromagnetic wave, therefore, is a derivation of equation of either **E** or **B** into the familiar wave equation. The wave equation for an electric field waveform propagating in vacuum has an electric form as (Justin et al., 2015):

$$\nabla^2 \boldsymbol{E} - \epsilon_0 \mu_0 \frac{\partial^2 \boldsymbol{E}}{\partial t^2} = 0 \qquad (2\text{–}41)$$

The solution of Maxwell's equations in sinusoidal form is called plane wave (Justin et al., 2015):

$$\boldsymbol{E}(\boldsymbol{r}, t) = \boldsymbol{E_0} cos(\boldsymbol{k} \cdot \boldsymbol{r} - \omega t + \varphi) \qquad (2\text{–}42)$$

In which, φ is an arbitrary (constant) phase term. The vector **k** is wave vector (Justin et al., 2015):

$$\boldsymbol{k} \equiv \boldsymbol{ku} = \frac{2\pi}{\lambda_{vac}}\boldsymbol{u} \tag{2–43}$$

$\boldsymbol{u}$ is unit vector defining the direction of propagation. λ_{vac} is the length that $\boldsymbol{r}$ must vary in direction of $\boldsymbol{u}$ to cause the cosine to go through a complete cycle. This distance is defined as the wavelength (Justin et al., 2015):

$$\omega = \frac{2\pi c}{\lambda_{vac}} \tag{2–44}$$

Where ω: angular frequency [Rad/s]

The wave equation require the satisfaction of the dispersion relation (Justin et al., 2015):

$$k = \frac{\omega}{c} \tag{2–45}$$

Where k: spatial frequency or wavenumber.

The corresponding magnetic field in sinusoidal form (Justin et al., 2015):

$$\boldsymbol{B}(\boldsymbol{r}, t) = \boldsymbol{B_0}\cos(\boldsymbol{k}\cdot\boldsymbol{r} - \omega t + \varphi) \tag{2–46}$$

The Faraday's law requires the cosine in equations **(2-42)** and **(2-46)** must be identical which indicate the electric and magnetic fields travel in phase. The Faraday's law also require (Justin et al., 2015):

$$\boldsymbol{B_0} = \frac{\boldsymbol{k}\times\boldsymbol{E_0}}{\omega} \tag{2–47}$$

This equation indicates that $\boldsymbol{B_0}$ is perpendicular to both $\boldsymbol{E_0}$ and $\boldsymbol{k}$**,** and Gauss's law force $\boldsymbol{E_0}$ perpendicular to $\boldsymbol{k}$**.** (Justin et al., 2015)**.** The association of electric field and magnetic field is represented in ***Figure 8***.

The plane wave is perpendicular to **k** and can be acknowledged as a series of infinite sheets, each with a different uniform field strength moving in k direction. (Young and Freedman, 2016)

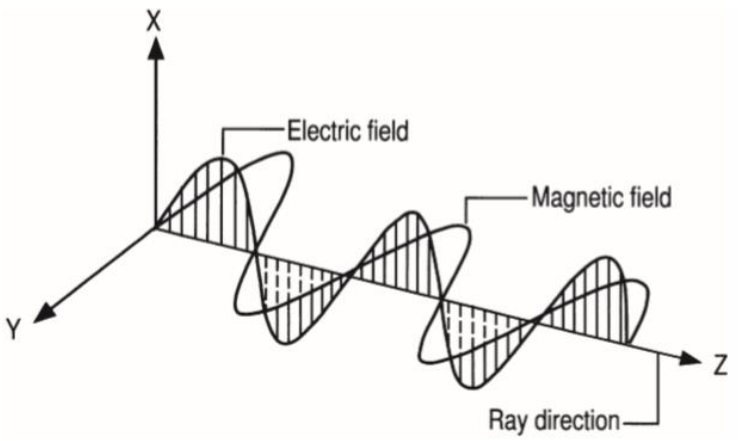

***Figure 8**: The electric and magnetic fields of a linearly polarized wave (Chen, 2000).*

2.3.3 Refraction

The speed of light in vacuum is c (299,792,458 m/s). However, when light travels from one medium to another, its speed experiences another value due to the change in speed of wave propagation. The ratio of the speed in the surrounding medium (c_a), to the speed in the substance (c_s) is defined by n_s- index of refraction (Budynas, 1999):

$$n_s = \frac{c_a}{c_s} \tag{2–48}$$

2.3.4 Polarization

Light rays mostly emitted from light sources which consist of a large number of randomly oriented atomic or molecular emitters having no preferred orientation. Such light has a random vibratory motion in a plane transverse to the direction of propagation. When the direction of the electric field of light oscillate in a regular and predictable manner, the light is defined as being polarized. The direction of the oscillating electric field is described by the concept of polarization. If the electric field oscillates in a plane, the light is linearly polarized. As the electric field oscillates spiral around while a plane wave propagates, the light is defined as being circular or elliptical polarized. (Justin et al., 2015)

The polarized light was first studied by Erasmus Bartholinus in 1669. He was the first modern scientist introduced this phenomena which was observed as the double images when seeing through a calcite crystal, a form of calcium carbonate ($CaCO_3$) also called Iceland spar. In the historical review, the Vikings may have taken advantage of these

crystals for navigation by observation of the polarization in the sky. Yet, this early work did not fully explain the phenomena until after the work of Maxwell in 1873. The polarization of light, then, was explained as one of the basic properties of light wave and is defined to be the description of the vibration of the electric field. (Goldstein, 2011)

The concept suggested that light was not a scalar quantity was first presented by Christian Huygens through his work on the propagation of light through crystals. The vectorial nature of light, then was termed polarization which has three independent oscillations or optical disturbances described by three independent wave equations (Goldstein, 2011):

$$E_x(\boldsymbol{r},t) = E_{0x}\cos(\omega t - \boldsymbol{k}\cdot\boldsymbol{r} + \varphi_x),$$
$$E_y(\boldsymbol{r},t) = E_{0y}\cos(\omega t - \boldsymbol{k}\cdot\boldsymbol{r} + \varphi_y), \quad (2\text{–}49)$$
$$E_z(\boldsymbol{r},t) = E_{0z}\cos(\omega t - \boldsymbol{k}\cdot\boldsymbol{r} + \varphi_z).$$

Where: **r**: **r** (x, y, z).

$E_x(\boldsymbol{r},t)$ and $E_y(\boldsymbol{r},t)$: the transverse components

$E_z(\boldsymbol{r},t)$: the longitudinal component when the propagation is in the z-axis.

However, in 1818, the work of Frenel and Arago had proved the longitudinal component equation did not exist and light consists of only transverse components. If the z-axis is taken as orientation of the direction of propagation **k**, the optical field in free space must be described by (Goldstein, 2011):

$$E_x(z,t) = E_{0x}\cos(\omega t - kz + \varphi_x) \quad (2\text{–}50)$$
$$E_y(z,t) = E_{0y}\cos(\omega t - kz + \varphi_y) \quad (2\text{–}51)$$

Where E_{0x}, E_{0y}: are the maximum amplitudes,

φ_x, φ_y: the arbitrary phases,

$(\omega t - kz) = \tau$: propagator.

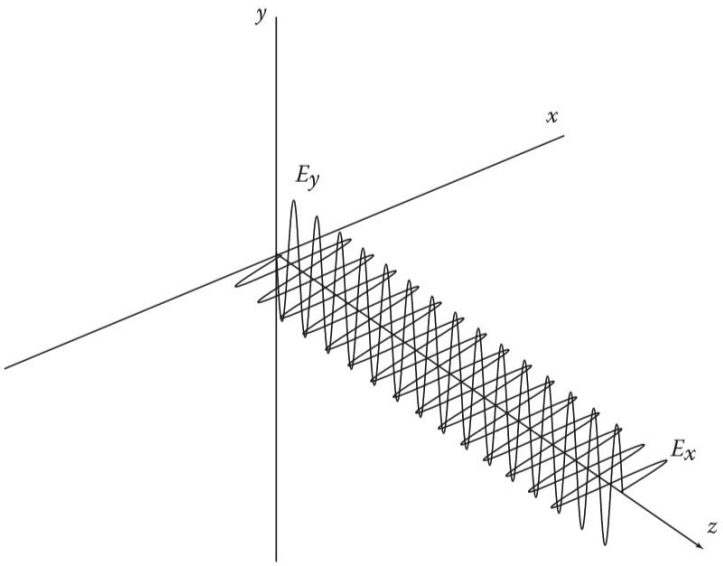

***Figure 9**: Propagation of the transverse optical field (Goldstein, 2011).*

The subscripts x and y refer to the components in the x and y directions. As the field propagates, component E_x and E_y give rise to the resultant vector (Goldstein, 2011):

$$\boldsymbol{E} = \boldsymbol{E}_x + \boldsymbol{E}_y \tag{2–52}$$

Linearly polarized light is defined to have its polarization axis oriented in any direction in the x-y plane consisting of two components oriented along the x and y axes, respectively. The polarization axis orientation is determined by the relative magnitudes of the two components which share a same frequency ω and an absolute phase $\varphi = \varphi_x = \varphi_y$. In this case the light has its component oscillating only in the x direction ($E_{0y} = 0$ and $E_y(z,t) \neq 0$), the light is said to be linearly polarized in x direction or horizontally polarized light. Similarly, the component of light oscillates only in y direction, the light is termed linear vertically polarized light. (Goldstein, 2011)

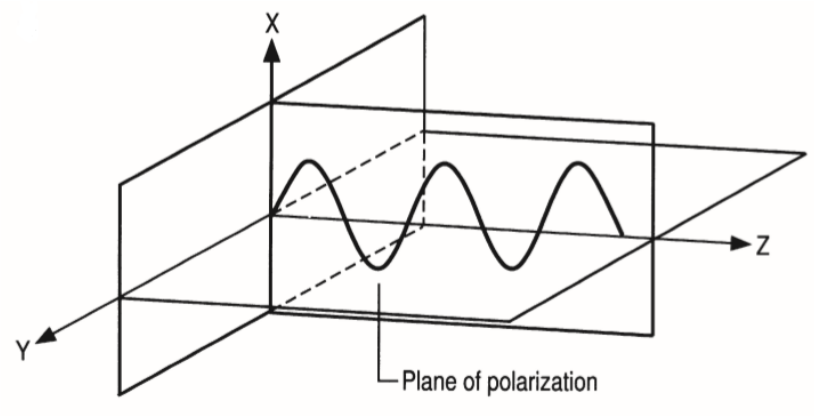

***Figure 10**: Motion of the plane or linear polarized light vectors (Chen, 2000).*

The circular polarization is a special case that the light has an identical amplitudes but 90^0 out of phase $\varphi_0 = \varphi_y = \varphi_x \pm \frac{\pi}{2}$. The resultant electric field then become (David et al., 1990):

$$\boldsymbol{E} = \boldsymbol{E}_x + \boldsymbol{E}_y = E_0\{\sin[\omega t - kz + \varphi_y]\,\boldsymbol{i} + \sin[\omega t - kz + \varphi_y + \pi/2]\boldsymbol{j}\}$$

$$= E_0\{\sin[\omega t - kz + \varphi_y]\,\boldsymbol{i} + \cos[\omega t - kz + \varphi_y]\boldsymbol{j}\} \quad (2\text{–}53)$$

Or

$$\boldsymbol{E} = \boldsymbol{E}_x + \boldsymbol{E}_y = E_0\{\sin[\omega t - kz + \varphi_y]\,\boldsymbol{i} + \sin[\omega t - kz + \varphi_y - \pi/2]\boldsymbol{j}\}$$

$$= E_0\{\sin[\omega t - kz + \varphi_y]\,\boldsymbol{i} - \cos[\omega t - kz + \varphi_y]\boldsymbol{j}\} \quad (2\text{–}54)$$

Observing in z-axis, the vector representing the electric field of the light changes in time, in consequence, the tip of the vector plots out a circular path over time.

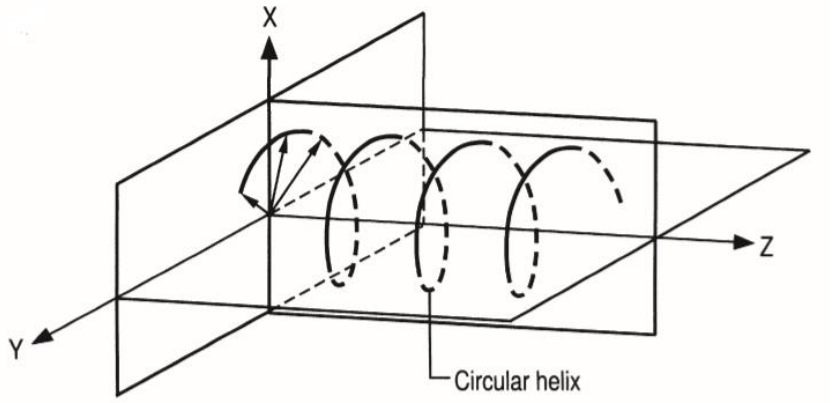

***Figure 11**: Motion of the circular polarized light vectors (Chen, 2000).*

Linear polarization and circular polarization are two special cases of polarized light, if the component combined do not meet these criteria, then it belongs to elliptically polarized light. Elliptical polarized light can be thought of a combinations of linearly of circular polarized components. Vector resultant of two out of phase linear components results in elliptically polarized light. If the two linear components having identical amplitudes are out of phase by π/4, the resultant light is circularly polarized. (David et al., 1990)

2.3.5 Linear Polarizer and Quarter-wave Plate

Linear polarizer or plan polarizer is a device used to transmit a beam of light whose electric field vector oscillates in a plane containing the beam axis. The orientation of the plane in space can be varied by rotating the polarizer about the beam axis. For instance, a horizontal linear polarizer allows the electric field component of incident light having a same transmission direction passing through, the perpendicular ones are absorbed, reflected, or deflected, depending on a particular scheme. A pair of ideal polarizers whose transmission axes are perpendicular (or crossed) to each other will completely extinguish an incident light. (David et al., 1990)

A quarter-wave plate ($\lambda/4$) is a special retarder which increase the phase of one linear polarization by 90° relative to the other. ***Figure 12*** shows the states of polarization of light passing through a $\lambda/4$ plate. The fast axis is located in the horizontal plane and the linearly polarized light has the azimuth varies from $\theta = 0^o$ to $\theta = 90^o$. When $\theta = 0^o$, the state of polarization of the beam remains the same since only the ordinary passes though the plate. As $\theta = 15^o$, the transmitted light is elliptically polarized with the ellipse's major axis lying along the fast axis of the $\lambda/4$ plate. For the value of $\theta = 45^o$, the transmitted ray is right circularly polarized. As the value of θ is increasing from $45^o - 90^o$, the light is again elliptically polarized, however, the major axis of the ellipse lying along the direction of the slow axis of the $\lambda/4$ plate. The transmitted light is again linearly polarized and plane of propagation coincides with the slow axis when $\theta = 90^o$. (Bannett, 1995)

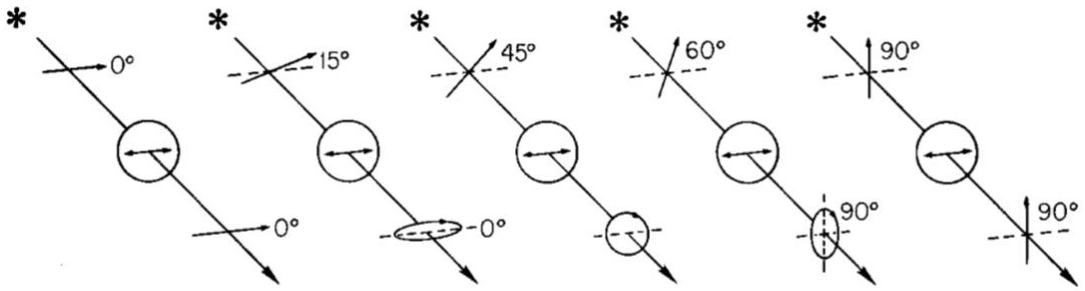

***Figure 12**: State of polarization of a light wave after passing through a $\lambda/4$ plate (whose fast axis is indicated by the double arrow) for different azimuths of the incident plane-polarized beam. (Bannett, 1995)*

2.3.6 Stress and Birefringence

A randomly oriented light ray entering an anisotropic medium will splits into two linearly polarized beams. One of the beams obeys Snell's law of refraction and is acknowledged as the ordinary ray. The second beam generally does not obey Snell's law, then is known as the extraordinary ray. These two waves are linearly polarized and propagate with different wave velocity (or phase velocity) and ray velocity, and their planes of polarization are perpendicular to each other. The ordinary and extraordinary rays, hence, are characterized by different refractive indices. This phenomenon is acknowledged as double refraction, or birefringence. (Bannett, 1995) If the incident rays are parallel to the optic axis, these two rays have the same refractive index and behave as though they travel through an isotropic medium obeying Snell's law. Conversely, when the incident light is perpendicular to the optic axis, the extraordinary ray travels faster than the ordinary one due to its lower refractive index and travel in the same direction. The ordinary ray travels undeviated and is refracted according to Snell's law, while the extraordinary one deviates from ordinary ray with the direction away from the optic axis, generally out of the plan of incidence. (Ramesh, 2000)

A certain transparent material behaves as a birefringent plate as being stressed, in which the value of the principal indices of the refraction n_1 and n_2 are directly related to principal strain. Due to the relationship of stress and strain, the retardation can be used directly to determine the stresses. The method is called photoelasticity. (James F. Doyle and James W. Phillips, 1989). In the photoelastic experiment, an incident ray is set to be perpendicular to the optic axis. The principal stress directions turn into a polarising axis at the point

of interest. The ordinary and extraordinary rays travel in the same direction but with different velocities, then are polarised with the polarising axes are perpendicular to each other. There exists a relative retardation between the transmitted rays, which contribute to the formation of fringes. (Ramesh, 2000)

Consider a birefringent material and a constant thickness t, in a state of plane stress where at a point in plane observed principal stresses σ_1, σ_2 (σ_3=0 as the third principle stress is perpendicular to the plane). The difference is those principal stresses is directly related to the difference in the indices of refection (Ramesh, 2000):

$$n_1 - n = c_1\sigma_1 - c_2\sigma_2 \quad (2\text{–}55)$$

$$n_2 - n = c_1\sigma_2 - c_2\sigma_1 \quad (2\text{–}56)$$

Where n_1, n_2: refractive indices for vibrations corresponding to these two directions

n: refractive index in the unstressed state

c_1: direct stress-optic coefficient

c_2: transverse stress optic coefficient

Let $C = c_1 + c_2$, the equation becomes (Ramesh, 2000):

$$N = \frac{\delta}{2\pi} = t\frac{C}{\lambda}(\sigma_1 - \sigma_2) \quad (2\text{–}57)$$

Where C: stress-optic coefficient

t: material thickness

δ: phase difference ($\delta = \varphi_x - \varphi_y$)

N: photoelasticity fringe order (N=0,1,2,3..)

The equation (2-57) can be written as:

$$\sigma_1 - \sigma_2 = \frac{NF_\sigma}{t} = \frac{N\lambda}{Ct} \quad \textbf{[Stress optic law]} \quad (2\text{–}58)$$

Where $F_\sigma = \frac{\lambda}{C}$: material stress fringe value [N/mm/fringe]

The material stress fringe value determination is identified as calibration of a photoelastic material. Stress fringe value of materials has to be evaluated with at least two to three

decimal places accuracy, as it is the only parameter which links the optical information to stresses. (Ramesh, 2000)

2.4 Injection Moulding

Injection moulding is the most commonly used manufacturing process for the plastics parts. Products produced from this technique vary in their size, complexity, and application with good dimension accuracy and surface finishing. The process required the use of an injection moulding machine, raw plastics material in shape of power, granules or pellets, and a mould. (Subramanian, 2015)

There are two types of injection moulding machines which are ram and screw injection moulding machines. Ram injection moulding machines were used for manufacturing moulded parts in earlier. However, this technique owns disadvantages of poor plasticization, inadequate mixing, and thermal gradient in melt causing inconsistent flow behaviour. Other disadvantages are pressure differences and cycle varies caused by variable injection pressure. Screw injection moulding, on the other hand, provides fast plasticization and decreased cycle time. This type of machine operates as the screw rotating and axially reciprocating by hydraulic motor; therefore, the materials are melted, mixed and pumped into mould cavity. (Subramanian, 2011)

2.4.1 Machinery

An injection moulding machine contains an injection and plasticization unit, mould clamping unit, and hydraulic and control unit. The polymer is melted by heating and shearing in injection unite then injected under pressure into a mould cavity, which is held by the mould clamping unit. The molten polymer then solidifies into a shape of the mould cavity when it is cooled. The injection unit is manipulated by the hydraulic unit. The whole process including overall control and sequences of the machine are functioned by control unit. (Subramanian, 2011)

The injection unit consists of barrel, ram or screw, and nozzle. This unit is responsible for both heating and injection the material into the mould. Procedure starts with the granules poured into a hopper, which is a large container with open bottom. The raw materials then melt in the barrel under its mechanism of heating and shearing force of the screw. The barrel is made of a steel cylinder that contains a reciprocating screw. A reciprocating screw moves material forward by both rotating and sliding axially to inject into the mould cavity through the nozzle at the end of the barrel. Once materials have solidified inside the mould, mould opens, ejection pins release part from the mould, the screw can retract and fill with material to prepare for the next shot. Mould operates under clamping unit, which provides the motion needed to hold mould together, opens and closes it automatically, and ejects the ready part. A hydraulic unit is responsible for pumping, motors, actuators, valves, piping, and so forth, which consist of hydraulic components with system pressure and is controlled by proportional valve. (Subramanian, 2011)

2.4.2 Mould

Mould in injection moulding is a complex tool which is high cost and time effective at their design and manufacturing stages. Every mould consists of two halves that brought together and clamped, and a cooling channels to help maintain a constant temperature throughout the tools. In mould design, it is required to pay attention on mould size, number of cavity, cavity layouts, runner systems, gating systems, shrinkage, and ejection system. It is important that the mould must allow the molten plastic to flow easily into all of the cavities. Therefore, the surface of mould cavity is required to be smooth and high polished, as well as avoided sharp corners and sudden changes in wall thickness in order to prevent the interruption of plastics flow and mould weakening. Deep shapes must be tapered to help in moulding removal. Ejector pins are built into the mould to push the moulding out. Mould gate or gates connects runner to the part that decide a part quality and productivity. The gate design includes selection of type, dimension and location which are driven by material, filler, economic factors, mould design and the part specifications. In injection moulding, the mould runner system is one of the most important factors which influents the process and properties of parts. Runners are used to convey the plastic melt from the sprue to the gate, then into the mould cavities. They can be full round, half round and trapezoidal. The length and diameter of runners decide the amount

of material in the moulding process. The sprue functions as delivering melted plastic into the mould with the size required to be larger than the maximum wall thickness of the moulded part and must be moulded easily and readily. Mould cavity is an important factor influent on moulded parts and desired precision form. By adjusting correlative parameters during filling, cavity directly controls the injection moulding process. The cavity is required to be well vented to allow the trapped gases and air to escape with all plastics to avoid the flow fronts apart. Nozzle includes open and needle shut-off nozzle which help melted plastics pumped into the mould. Vent function as releasing the air inside the cavity as mould closes. Ejection system is to deal with the frictional forces develop during ejection between the polymer surface and the surface of the mould and to help in part removal. (Subramanian, 2011). An injection moulding process goes through five stages:

- Mould close
- Filling stage
- Packing stage
- Holding stage
- Mould opening.

2.4.3 Injection Moulding Parameters

Injection moulding parameters include melting temperature, mould temperature, injection pressure, injection velocity, injection time, packing time, cooling temperature, and cooling time, play an important role in part quality. It is important to maintain the mould temperature at 40-50^{0}C or more since it decides the balance between part quality and productivity. Pressure in injection moulding varies from three sections: injection, hold, back which applies in both injection unit and clamping unit. The applied force is required to be high enough to keep the mould from material injection at maximum pressure and speed and proportionally related to the projected area of a part including the areas of runner and sprue. Time distributes in a cycle of injection moulding rank from 10 to 100 seconds, depending on the product size and cooling time. The cycle consists of three stages: feeding, stop, and injection. Cooling is a primary stage in injection moulding, comprises mould cooling and part cooling. Cooling time which take up to 70% to 80% of the entire cycle time, decides the productivity, quality of the products. (Subramanian, 2011)

Injection velocity is also an important key in thermoplastic injection moulding driven by polymer melt viscosity which is influenced by shear rate, temperature, molecular weight, and pressure. (Subramanian, 2011) In additions, part design also affects the processing due to its shape and dimension.

3 METHOD

3.1 Material

Polyethylene terephthalate (PET) is a thermoplastic material which owns a long chain polymer. PET is found in a vast array of applications within the packaging field, especially in food and beverage packaging. In pure form, PET is transparent, amorphous glass-like, and very light weight. The refraction index of PET is 1.5045 at 20^0C a wavelength of 5,893 A˚ (Bryan & Ray, 2009).

3.2 Samples Preparing by Injection Moulded

PET pellet was dried to eliminate the presence of water before being injection moulded. The dehydrating process was performed by P-Dry- FMD-MM-25-40-v. PET was dried thermally at temperature of 80^0C for 4 hours.

The samples were injection moulded by Engel-ES 200/25HL CC88 through two gate mould. The dried PET pellets was conveyed into injection moulding hopper right after the dehydrating process was done. Melting temperature was set at 225^0C in the last section of the screw and 235^0C at nozzle. The mould temperature was kept at 50^0C, samples were allowed to be cooled for 55 seconds.

3.3 Tensile Testing

The properties of PET are represented **Appendix II** with dimension in millimetre shown in ***Figure 13*** based on the standard of ASTM D638. A hole with diameter of 1, 2, 3, 4, and 5 mm was drilled on sample test pieces as shown in ***Figure 14***: Tensile testing specimens.

The tensile testing was performed by Testometric M 350- 5CT at room temperature of 20^0C with extension rate of 25 mm/min. The specimen was gripped into two apparatuses so that it was equally spaced and was clamped vertically. The distance of 50 mm was set between the grips. The data was gathered and loaded into a spreadsheet.

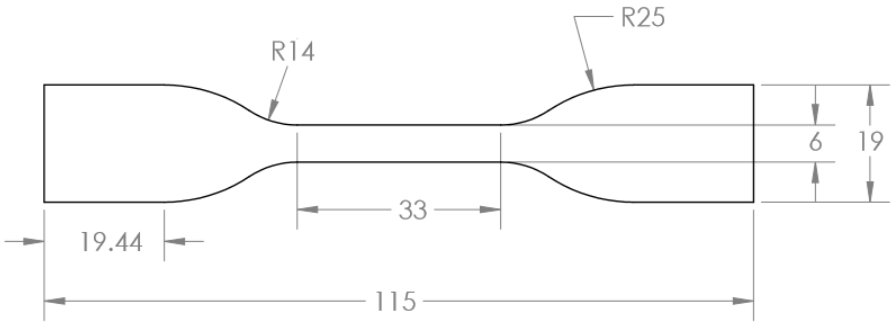

***Figure 13**: Specimen dimension*

***Figure 14**: Tensile testing specimens*

3.4 Comsol Model

Comsol models were built based on a simple static structural analysis with the purpose of demonstrate how materials with holes react to loads. The models used the Solid Mechanics with boundary load feature in one end and fixed constrain in other end of the body to examine the material behaviour under load. Stationary study was selected by the assumption that the load, deformation, and stress do not vary in time. Model geometry is shown in ***Figure 13*** with input parameters shown in table below:

***Table 1**: PET's input parameters.*

Name	Value	Unit
Density	1380	kg/m^3
Young's modulus	2757000000	Pa
Poisson's ratio	0.44	1

Boundary load governing equation:

$$\mathbf{S} \cdot \mathbf{n} = \mathbf{F}_A$$

$$\mathbf{F}_A = \frac{\mathbf{F}_{tot}}{A}$$

A total load with magnitude of 1000N was applied in one end of the component. For the other end, fixed boundary was set to constrain the displacement of each point on a boundary surface to be zero in all directions.

***Table 2**: Load description*

Description	Value
Load type	Total force
Total force, x component	-1000
Total force, y component	0
Total force, z component	0

Extra fine mesh was used. Mesh setting determines the finite element mesh resolution that is used to discretize models. The total small elements for this non-hole model are shown in ***Table 3***. By each element, a set of polynomial functions is built to approximate the structural displacement field in each of the three coordinate direction.

***Table 3**: Mesh's statistics and size.*

Description	Value
Minimum element quality	0.2075
Average element quality	0.6169
Tetrahedral elements	2879
Triangular elements	2056
Edge elements	272
Vertex elements	32

Description	Value
Maximum element size	4.03
Minimum element size	0.173
Curvature factor	0.3
Resolution of narrow regions	0.85
Maximum element growth rate	1.35
Predefined size	Extra fine

3.5 Photoelasticity Setup

The setup order of the optical elements in a plane polariscope is represented in the work of Terry Y. Chen, 2000. The setup consists of two linear polarizers, one acts a polarizer and the other acts as an analyser, and a white light source. The polarizer is set to have a vertical optical axis and analyser has a horizontal optical axis. The sample is place in the between two polarizers as shown in ***Figure 15***. This arrangement is to measure the principal stress directions that occur when polarized light passes through a stressed birefringent model. In this thesis work, unstressed models were exterminated with the objective of determining the available stresses in the models after being drilled.

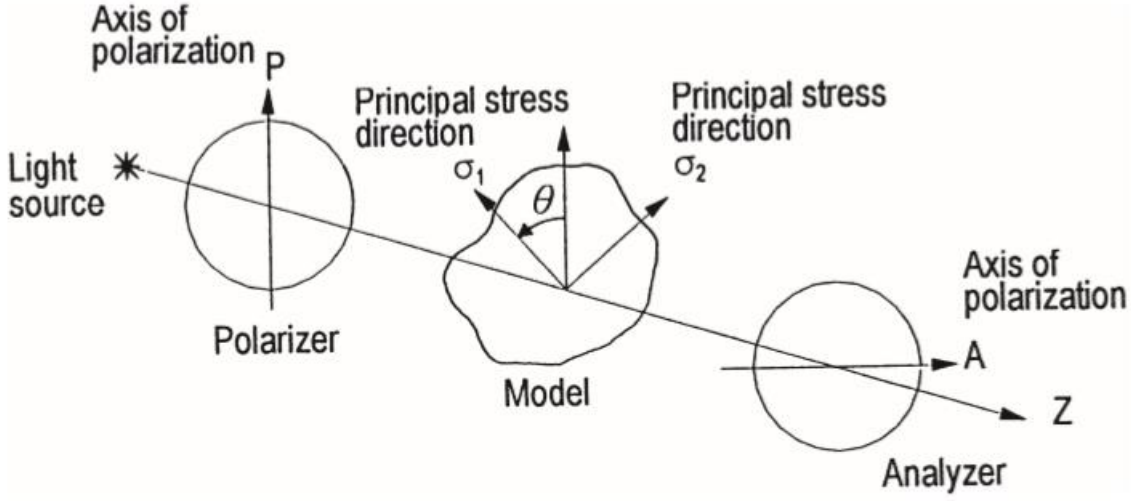

Figure 15*: Arrangement of the optical elements in a plane polariscope. (Chen, 2000)*

At the point of interest in the model, the principal stress direction makes an angle θ with the polarization axis of the polarizer. The plane polarizer emerges the incident light wave into a plane-polarized light wave, then this light wave enters the stressed model and is resolved into two components E_1 and E_2. The two components vibrate parallel to the principal stresses direction $\sigma_1$and σ_2 at the point of interest. (Chen, 2000)The velocities difference between two components causes the waves emerging from the model to have a relative phase shift between them.

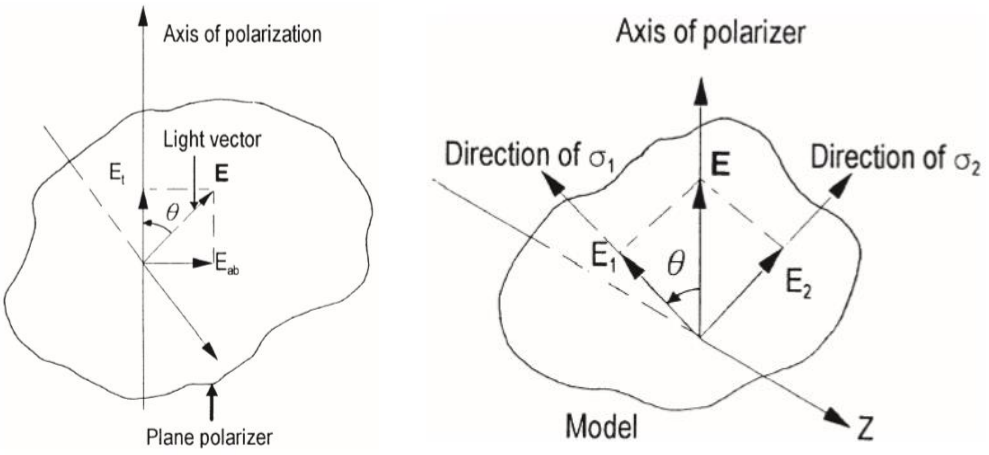

***Figure 16**: Transmitting and absorbing characteristic of a plane polarizer and in a stressed photoelastic model. (Chen, 2000)*

The analyzer combines the resolved light components emerging from the stressed photo-elastic model into a plane-polarized light vector.

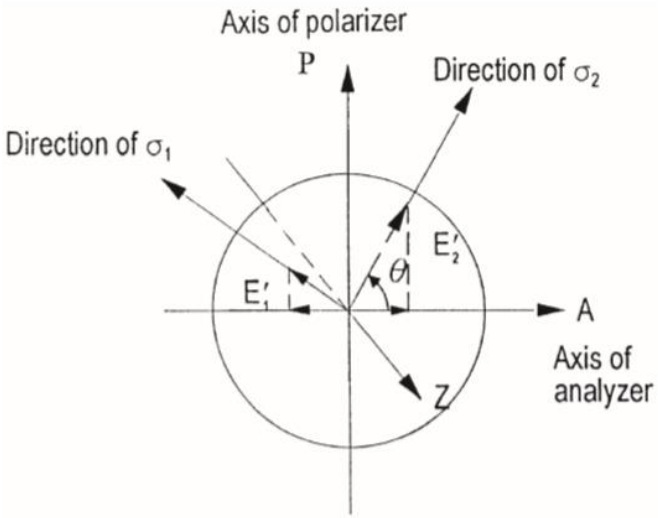

***Figure 17**: Transmission of the components of the light vectors through the analyzer. (Chen, 2000)*

Under monochromatic light, the isochromatic fringe pattern can be obtained as a series of dark bands, while white light causes the isochromatic fringe pattern to appear as a series of colored bands (Chen, 2000). As the principal stress difference is zero, the black fringe appears. However, this plane polariscope setup brings the isoclinic fringes and the isochromatic fringes to be superimposed at the same time.

4 RESULTS

4.1 Mathematical Analysis

The specimen without a hole lies in the x, y plane and was loaded in x direction at one end with the magnitude of 1000 N. The state of stress is plane stress, consequently, the stress components $\sigma_z,\ \tau_{xz}, \tau_{yz} = 0$.

The Mohr's circle for uniaxial loading is shown in ***Figure 19***, with normal stress on a cross section is:

$$\sigma_x = \frac{P}{A} = \frac{1000\ [N]}{(6 \times 2)[mm]} = 83.33\ [MPa]$$

In the formula above, the normal stress distribution over the normal plane to the axis is calculated by the force distributed over the face (P) divided by normal cross area (A) over that face. The normal stress in y direction σ_y is equal to zero since there is no external force acting in y direction. The stress tensor of principal stress has the form:

$$[\sigma] = \begin{bmatrix} \sigma_x & 0 & 0 \\ 0 & 0 & 0 \\ 0 & 0 & 0 \end{bmatrix} = \begin{bmatrix} 83.33 & 0 & 0 \\ 0 & 0 & 0 \\ 0 & 0 & 0 \end{bmatrix} MPa$$

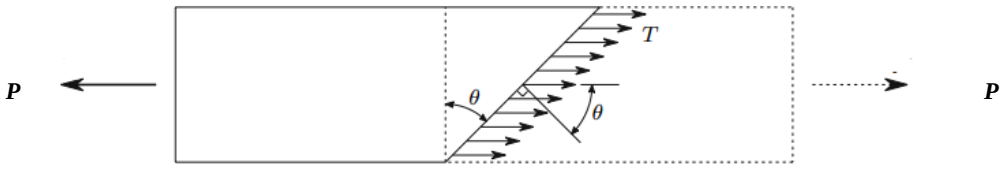

Figure 18: *Stresses in an inclined section (Silva, 2006).*

Looking at the stress distribution over the plane inclined an angle φ to that normal plane, by exanimating the equilibrium condition of two separating parts of the body, the area over the inclined proportion is given by A over the Cosine φ:

$$A_{inclined} = \frac{A}{cos\varphi}$$

Therefore, the stress distribution over the inclined face is given by the force distributed over that face. The relationship of the inclined stress (T) with normal stress is:

$$T = \sigma_x cos\varphi$$

As consider the components of S on the inclined surface $A_{inclined}$, there exists two components: normal component and shear component.

$$\sigma_\varphi = Tcos\varphi = \sigma_x cos^2\varphi$$

$$\tau_\varphi = Tsin\varphi = \sigma_x cos\varphi sin\varphi = \frac{\sigma_x}{2} sin2\varphi$$

The angle φ runs from 0^0 to 90^0. The maximum normal stress is obtained when the angle φ is 0^0:

$$\sigma_{\varphi max} = \sigma_x$$

Maximum shear stress is obtained when $sin2\varphi = 1$, or when $\varphi = \frac{\pi}{2}$. In other words, maximum shear stress is 45^0 to normal stress in uniaxial tension. The normal stress is either maximum or minimum on planes for which the shearing stress is zero. Mohr's circle for uniaxial tensile load has a radius of $\frac{\sigma_x}{2}$ and centre at $(\frac{\sigma_x}{2}, 0)$.

For other specimens, the calculation method is similar, however, the area of the cross section is a multiply of specimen's width (H) after minusing the hole diameter (d) with its width (h): $A = (H - d)h$.

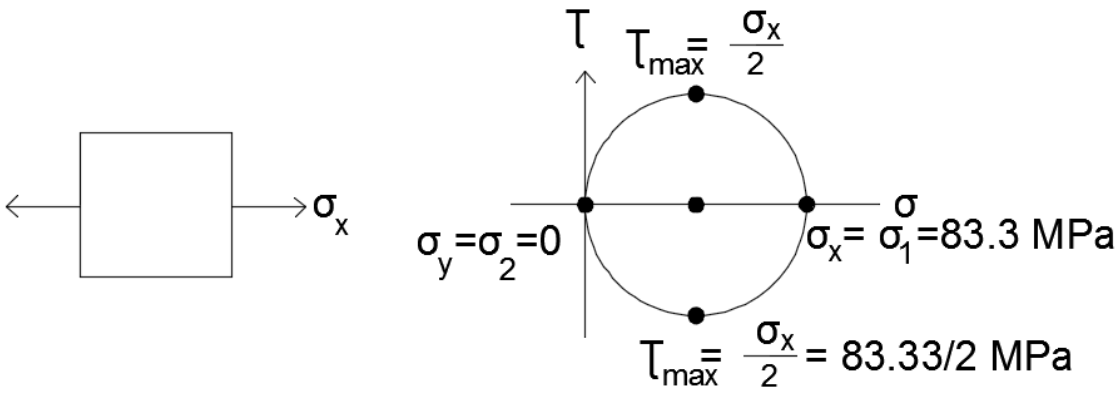

***Figure 19**: Mohr's Circle for uniaxial tension.*

The two stress concentration factors K_{tg} and K_{tn} derived theoretically for sample with different d/H ratio are represented in ***Table 4*** (Data was obtained from **Appendix I**). As the hole becomes larger, the ratio d/H increases from 0 to 0.83, K_{tg} increases from 1 to 30.22, nevertheless K_{tn} drops from 3 to 2.04. Nominal stresses were calculated by the equation (2-26), therefore, maximum stresses were obtained by equation (2-27). Maximum stresses can be obtained by either K_{tg} or K_{tn}, however, for simplicity, only K_{tn} was used to compared with other experimental results.

***Table 4**: Stress concentration factor for various d/H ratio.*

Samples	**1**	**2**	**3**	**4**	**5**	**6**
Load (P) [N]	1 000.00	1 000.00	1 000.00	1 000.00	1 000.00	1 000.00
Width (H) [mm]	6.00	6.00	6.00	6.00	6.00	6.00
Thickness (t) [mm]	2.00	2.00	2.00	2.00	2.00	2.00
Hole diameter [mm]	0.00	1.00	2.00	3.00	4.00	5.00
Net cross sessional area [mm²]	12.00	10.00	8.00	6.00	4.00	2.00
d/H	0.00	0.17	0.33	0.50	0.67	0.83
Nominal Stress [MPa]	83.33	100.00	125.00	166.67	250.00	500.00
Max. Stress [MPa]	250.33	258.39	289.22	359.50	519.22	1018.39
K_{tg}	1.00	1.90	3.47	6.31	12.23	30.22
K_{tn}	3.00	2.58	2.31	2.16	2.08	2.04

4.2 Tensile Testing

Uniaxial tensile tests were run on non-hole specimens with the goal of establishing base line properties to facilitate modelling efforts and comparison to geometries with holes. A comparison of theoretical stress concentration factor and fatigue notch factor has been performed. The notch sensitivity of PET was recorded by the work of Masaharu Takano and Lawrence E. Nielsen in 1976 (see **Appendix III**). In which, PET experiences a notch sensitivity run from 0.76 to 1.26 for various types of notches testing. A mean value of 0.98 was utilized in this work to calculate the fatigue notch factor, therefore, the limit of fatigue strength was predicted.

The results of tensile strength obtained from tensile experiments were graphed with tensile strength value derived from theory to visualize the comparison, and is represented in the ***Figure 20***. The vertical axis demonstrates the magnitude of tensile strength in MPa and the horizontal axis shows the ratio of holes' diameter over specimens' width.

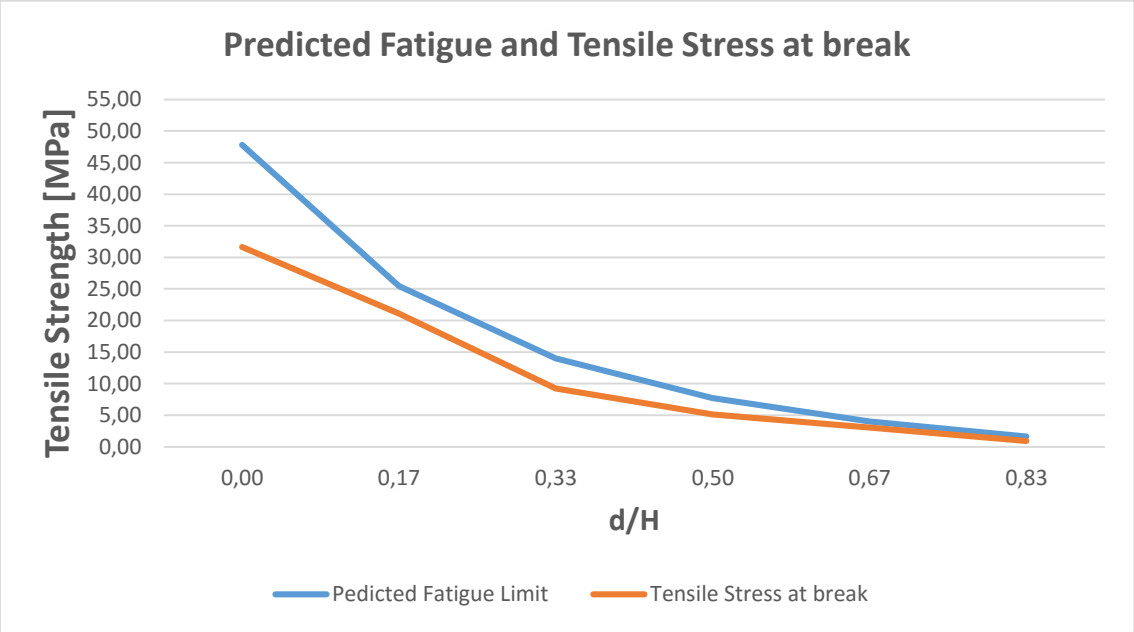

***Figure 20**: Tensile strength value by theory and practice.*

4.3 COMSOL Simulation

Mesh results from extra fine mesh setup specify a global element size and tolerance value. Mesh results consist of mesh elements for non-hole specimen and mesh condition around the hole of specimens with holes.

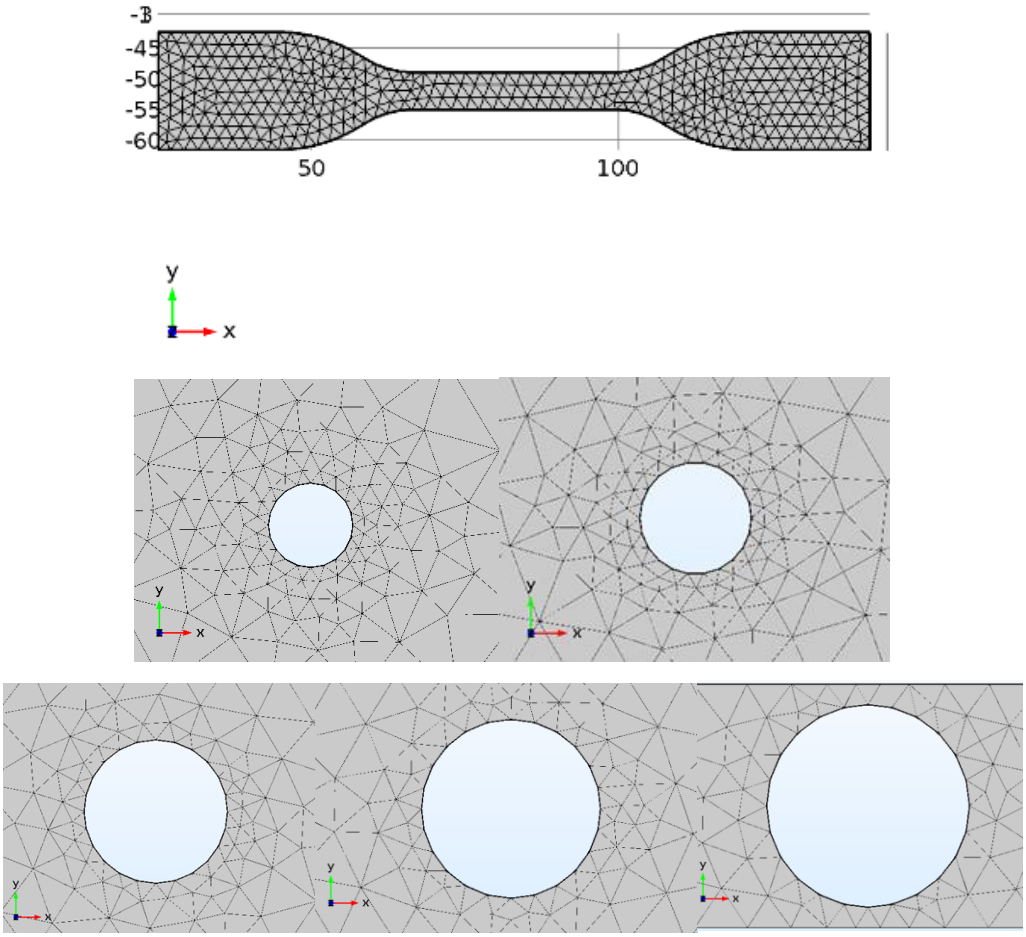

***Figure 21**: Mesh results of non-hole profile and profiles with hole of 1, 2, 3, 4, 5mm in diameter.*

Under the load of 1000 N in x direction, ***Figure 22*** shows the reaction of specimens subjected to the load by the contour maps of stresses acting on the cross section of the specimens. The results were contour in first principal stress in unit of MPa. The first principal stresses increase as the hole becomes larger. The maximum value of stress is recorded near the horizontal edges of the holes.

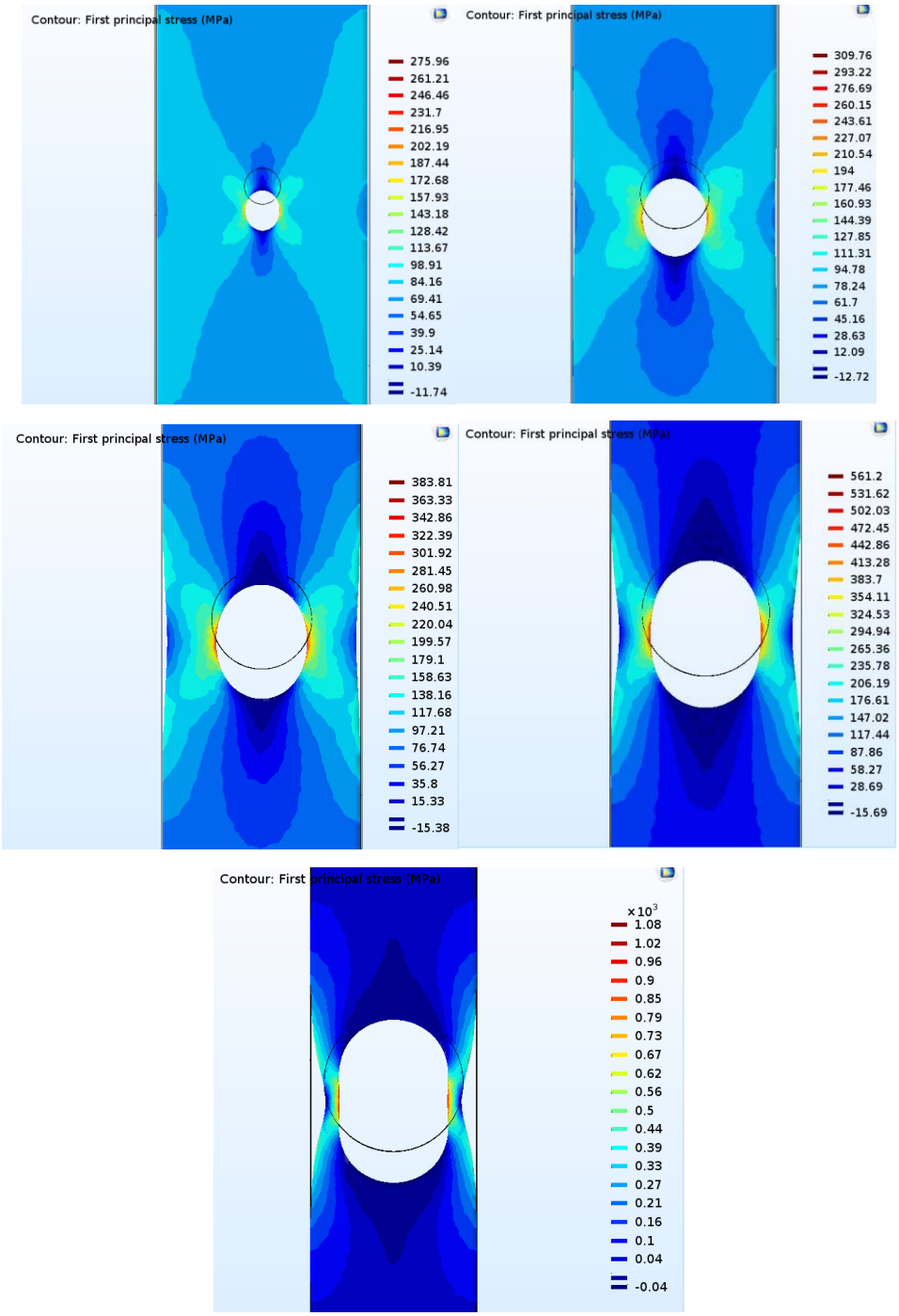

***Figure 22**: Computational results for profiles with hole of 1, 2, 3, 4, and 5 mm in diameter.*

The maximum stresses obtained from computational experiment provide a data to derive the stress concentration factor K_c. The stress concentration factor resulting from Comsol was calculated using equation (2-27) with the same nominal stress which was used to calculate maximum stress in section 4.1. Hence, a comparison of stress concentration derived from two methods was performed and represented in ***Figure 23***.

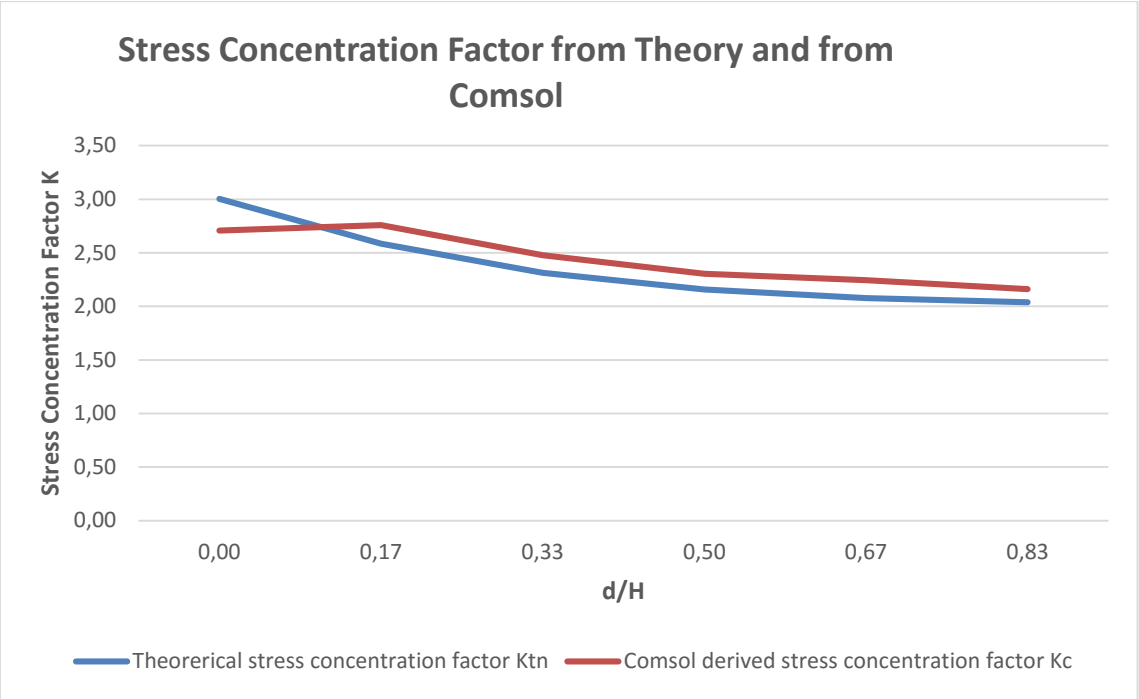

Figure 23: *Comparison of stress concentration factors derived from theoretical and computational methods.*

4.4 Photoelastic Observation

According to the birefringent theory, if the photoelastic model is free of stress, there is no double refraction, therefore, there is no stress concentration displaced. The results from photoelastic experiments which are represented in ***Figure 24*** illustrating the stress available in the samples under free of load. The photoelastic experiments were performed by plane polariscope arrangement which provided isochromatic and isoclinic superimposed at the same time. The specimens are thin flat plate and assumed to exhibit plane stress. The available of stress results in double refraction as the incident rays are perpendicular to the optical axis. However, the fringe pattern cannot be obtained from this experiment due to small stress level.

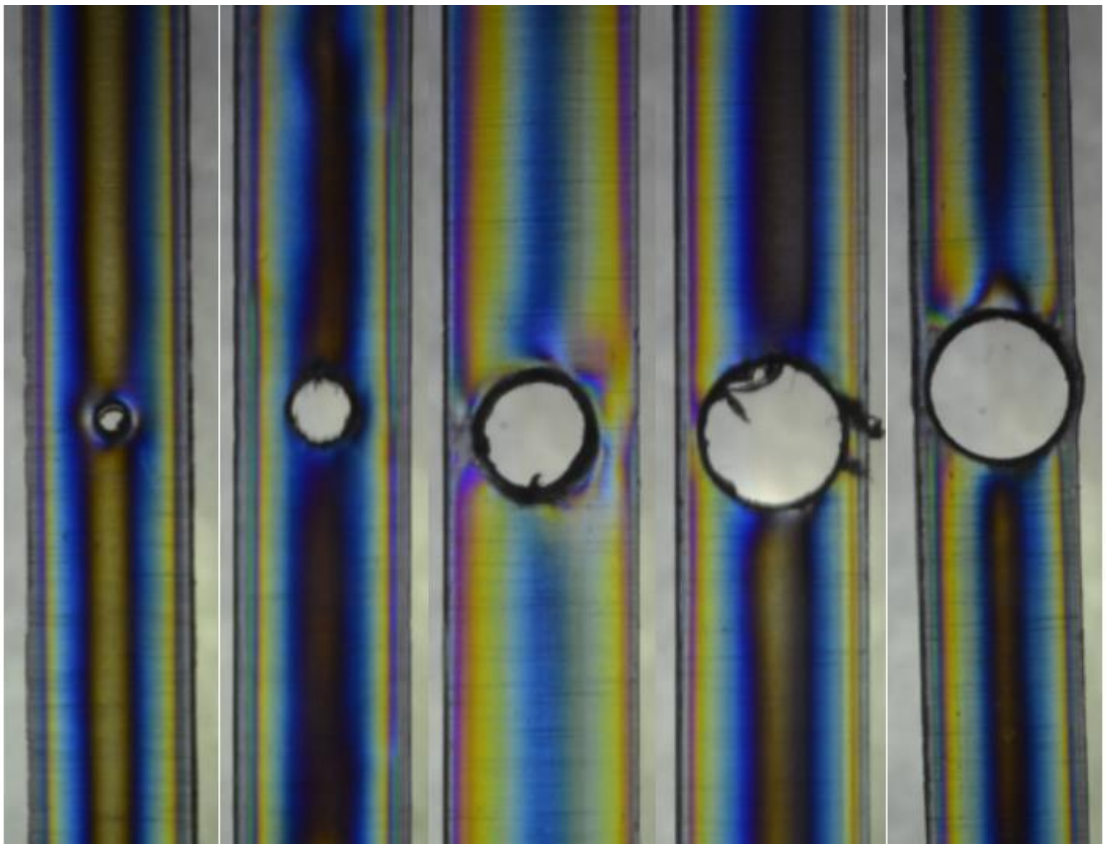

***Figure 24**: Photoelasticity observation for 1, 2, 3, 4, and 5 mm diameter-hole-samples in un-loaded state.*

5 DISCUSSION

5.1 Stress Concentration Factors

It can be seen that specimens in both cases with larger ratio d/H are more effected by the applied load due to high stress concentration factor and narrow area. As a hole is placed in the structural element causing a percentage of mass and flexural rigidity loses. The maximum stresses around the holes on y axis derived from computational methods are plotted in ***Figure 22*** having a higher trend compared to the maximum stresses obtained from ***Table 4*** by mathematical methods. The trend of stress concentration factor obtained from Comsol is similar to that of theoretical stress concentration factor, in which the line illustrating the magnitude of K_c lifts up around 6 % compared to line of K_{tn} when the present of holes exists. The value of K_c, however, is different from K_{tn}, which is 3 for structure without the present of holes. As the ratio of hole diameter over specimen's width increases from 0 to 0.83, K_{tn} decrease from 3 to 2.94, while K_c falls from 2.71 to 2.16. The higher maximum stress obtained from computational methods can be explained by the load and fixed constrain conditions. Since the load was applied in one end of the specimen and fixed constrain in the other end causing high stress concentration in the fixed part. This high concentration of stress near the fixed constrain position also explains for a value of 2.71 of K_c when there is no hole presenting on the element.

5.2 Fatigue Strength Predication

The two results obtained from ***Figure 20*** show a similar trend. The fatigue stress for non-hole element was recorded to have the highest magnitude in both cases, and gradually reduces as the diameter of the hole become larger. The errors existing between the two values have an average of 30 %, in which, theoretical fatigue strength has greater magnitude. The fatigue limit predicted for a sample without a hole was 47.81 MPa, which is 3.9 % error compared to theoretical tensile strength (See **Appendix II**). The present of a hole in the middle of specimen causes a significant reduce in its tensile strength. A specimen with the ratio of hole diameter over its width of 0.17 experiences a noteworthy drop of roughly 50 % in tensile strength compared to specimen without an existing of holes in both theoretical and experimental circumstances. The magnitude of material tensile

strength continues to reduce as the diameter of the holes become larger. The specimen with ratio d/H of 0.17 was predicted to have the failure occurs at 25.46 MPa compared to its theoretical fatigue strength of 48 MPa due to the presentation of 1 mm diameter hole. The experiment result recorded for this sample was 21.11 MPa, which is 17% lower than predicated value. The highest error of 44% occurred at the sample with largest hole. The predicted value was 1.61 MPa compared to 0.91 MPa of the tensile test.

Sample fabrication and testing procedure strongly affect the mechanical properties of the test pieces. The available of residual stress caused by shrinkage during cooling period of injection moulding can reduce the mechanical performance of final product. However, the consequent residual stresses from the mentioned process can be significantly small compared to one formed by hole drilling. The holes drilling left a significant deformation to the holes' neighbourhood as presented in ***Figure 24*** by photoelastic method. Observing around the holes, the surfaces are rough and low tolerance due to wear of machining equipment compared to ideal surfaces in theoretical method. Furthermore, since experimental method was performed with human interaction and by machined built by human, there always exist a certainty amount of errors. The input value of tensile testing machine was a mean value instead of exactly dimension of each specimen.

6 CONCLUSION

The main goal of the thesis is achieved by conducting experiments and observing stress concentration for samples with varied hole radius. Specimens with holes of different sizes cut in the middle was the target for calculation by theoretical method, and put into simulation for comparison. Additionally, photoelastic method was also set up for stress condition observing under load-free environment. The results of maximum stresses and fatigue strength from different hole size specimens show good correlation between theoretical, computational and experimental methods. There still exists some errors between those methods, yet they are explainable.

For further studies, since this thesis work just provided a simulation of maximum stress by Comsol Multiphysics, other program such as Matlab and Nastran should be explored. The stress concentration factor can be also derived by experimental method as the position of maximum stress can be studied by circular polariscope arrangement which can eliminate the present of isoclinic fringes and provide only isochromatic fringes. Apart from single circular hole, other geometry of cracks with different arrangements in structures are recommended to study.

REFERENCES

Anon., 2009-2016. *Everything.Explained.Today.* [Online]
Available at: http://everything.explained.today/Photoelasticity/
[Accessed 17 February 2016].

Bannett, J. M., 1995. Polarization. In: M. Bass, ed. *Handbook of Optics, Volume I: Fundamentals, Techniques, and Design, 2nd Edition.* s.l.: McGraw-Hill , Inc , pp. 5.1-5.8.

Bryan, E. & Ray, S. eds., 2009. Poly(ethylene terephthalate). In: *Polymers: A Properties Database, 2nd Edition.* s.l.:Taylor & Francis Group, LLC , p. 603.

Budynas, R. G., 1999. Experimental Stress Analysis - The Theory of Photoelasticity . In: *Advanced Strength and Applied Stress Analysis, Second Edition.* s.l.:McGraw Hill Companies, Inc., pp. 626-642.

Chen, T. Y., 2000. Digital Photoelasticity . In: P. K. Rastogi, ed. *Photomechanics* . s.l.: Springer-Verlag Berlin Heidelberg, pp. 197-230.

David et al., 1990. *Polarized Light in Optics and Spectroscopy.* s.l.:Academic Press, Inc..

Goldstein, D. H., 2011. *Polarizated Light, 3rd Edition.* s.l.:Taylor and Francis Group, LLC.

Goldstein, D. H., 2011. The Polarization Ellipse . In: *Polarized Light, 3rd Edition.* s.l.:Taylor and Francis Group, LLC, pp. 49-58.

James F. Doyle and James W. Phillips, 1989. *Photoelasticity.* s.l.:Society for Experimental Mechanics.

Javidinejad, A., 2015. Stress and Strain Relationship. In: *Essentials of Machanical Stress Analysis.* Boca Raton: Taylor & Francis Group, LLC, pp. 11-30.

Justin et al., 2015. *Physics of Light and Optics.* s.l.:Justin Peatross and Michael Ware.

Masaharu Takano and Lawrence E. Nielsen, 1976. The Notch Sensitivity of Polymeric Materials. *Journal of Applied Polymer Science,* Volume 20, pp. 2193-2207.

Ramesh, K., 2000. Transmission Photoelasticity . In: *Digital Photoelasticity: Advanced Techniques and Applications* . s.l.:Springer-Verlag Berlin Heidelberg , pp. 1-46.

Reddy, J., 2006. *An Introduction to the Finite Element Method.* 3rd ed. s.l.:McGraw-Hill.

Rösler et al., 2007. Elasticity. In: *Mechanical Behaviour of Engineering Materials: Metals, Ceramics, Polymers, and Composites.*. s.l.:Springer, pp. 31-60.

Silva, V. D. d., 2006 . The Strain Tensor . In: *Mechanics and Strength of Materials.* s.l.:Springer, pp. 41-64.

Silva, V. D. d., 2006. The Stress Tensor. In: *Mechanics and Strength of Materials.* s.l.:Springer, pp. 9-37.

Subramanian, M. N., 2011. Plastics Processing. In: *The Basics of Troubleshooting in Plastics Processing: An Introductory Practical Guide.* s.l.:John Wiley & Sons, Inc, pp. 61-87.

Subramanian, M. N., 2015. Injection Moulding. In: *Basics of Polymers: Fabrication and Processing Technology.* s.l.:Momentum Press®, LLC,, pp. 43-53.

Walter and Deborah , 2008. Definition and Design Relations. In: *Peterson's Stress Concentration Factors, Third Edition.* s.l.:John Wiley & Sons, Inc., pp. 1-54.

Walter and Deborah , 2008. Holes. In: *Peterson's Stress Concentration Factors, Third Edition.* s.l.:John Wiley & Sons, Inc., pp. 176-400.

Whitley, D. W., Fall 2013. *Interacting stress concentration factors and their effect on fatigue of metallic aerostructures,* s.l.: Missouri Univerity of Science and Technology.

Young and Freedman, 2016. Electromagnetic Waves. In: *University Physics with Modern Physics, 14th Edition.* s.l.:Pearson, pp. 1050-1072.

APPENDIX I

Stress concentration factors K_{tg} and K_{tn} for the tension of a finite-width thin element with a circular hole: (Walter and Deborah , 2008)

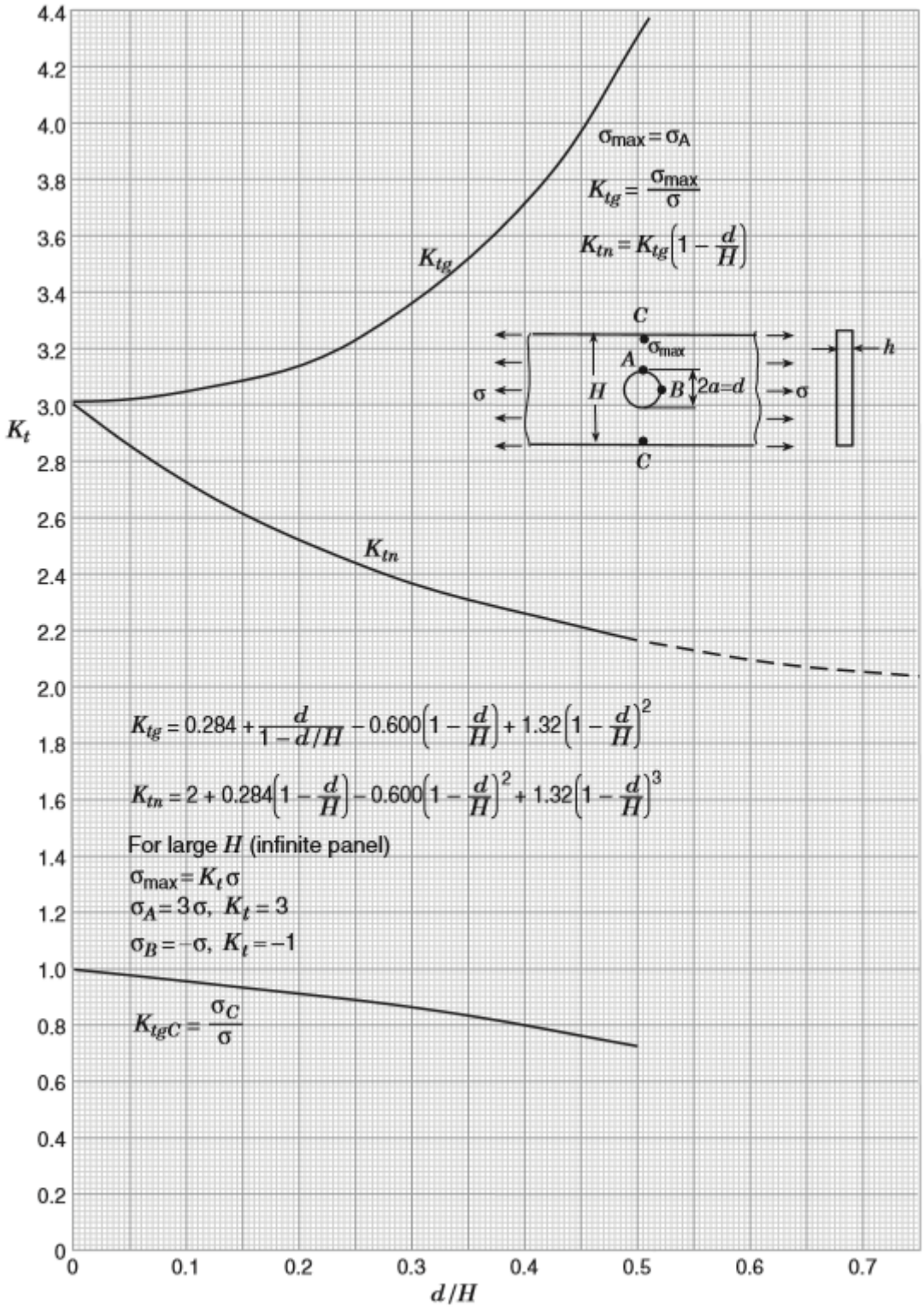

APPENDIX II

Polyethylene terephthalate properties: (Bryan & Ray, 2009)

Poly(ethylene terephthalate) P-271

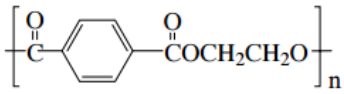

Synonyms: *PET. Poly(oxy-1,2-ethanediyloxycarbonyl-1,4-phenylenecarbonyl). Poly(oxyethylene oxyterephthaloyl)*
Monomers: Dimethyl terephthalate, 1,2-Ethanediol
Material class: Thermoplastic
Polymer Type: polyester
CAS Number:

CAS Reg. No.
25038-59-9

Molecular Formula: $(C_{10}H_8O_4)_n$
Fragments: $C_{10}H_8O_4$
Additives: Antioxidants (Irganox B-215 and 1098); compatibilisers (polypropylene-*graft*-maleic anhydride, polypropylene-*graft*-acrylic acid)

Mechanical Properties:

Tensile (Young's) Modulus:

No.	Value	Note
1	2757 MPa	400 kpsi, ASTM D638, amorph. [4]
2	4136 MPa	600 kpsi, ASTM D638, oriented film [4]
3	14100 MPa	oriented film
4	63 MPa	oriented film, transverse [11]

Tensile Strength Break:

No.	Value	Note	Elongation
1	48 MPa	7000 psi, amorph. ASTM D638 [4]	250–500%
2	248 MPa	36 kpsi, longitudinal [4]	60%
3	69 MPa	10 kpsi, transverse [4]	150%
4	172 MPa	25 kpsi, biaxially oriented, ASTM D638 [4]	100%
5	172 MPa	film [7]	

Poisson's Ratio:

No.	Value	Note
1	0.44	extension [11]
2	0.37	transverse [11]

APPENDIX III

Notch Sensitivity of Polyethylene Terephthalate (Masaharu Takano and Lawrence E. Nielsen, 1976)

TABLE V
Notch Sensitivity Factors for Strength

Plastics	Types of notches (Re. Table I) #1	#2	#3	#4	#5	#6
PMMA	3.26	2.62	4.71	2.68	2.64	1.64
PS	1.33	1.21	1.77	1.16	1.78	1.18
SAN	2.18	1.68	2.71	1.69	2.91	1.62
HIPS	0.92	0.87	1.01	0.84	0.93	0.83
ABS	1.01	0.92	1.10	0.92	1.04	0.96
HDPE	0.96	0.87	0.88	0.73	0.90	0.78
-annealed at 127°C for 72 hrs.	0.89	0.81	0.89	0.77	0.82	0.80
Polypropylene	1.04	0.92	1.30	0.93	1.15	0.91
Polyoxymethylene	1.00	0.87	1.26	0.94	1.18	0.86
Rigid PVC	0.97	0.92	1.03	0.84	1.03	0.88
Polycarbonate M-50	0.99	0.90	1.13	0.85	1.07	0.89
Polysulfone	1.61	1.50	2.36	1.44	1.15	0.93
PTMT	0.94	0.84	0.96	0.78	0.94	0.81
PET - transparent	1.02	0.90	1.26	0.85	1.11	0.76
- semi-transparent	1.00	0.88	1.34	0.83	1.29	0.80
Teflon - 0°	0.91	0.86	0.94	0.83	0.90	0.84
- 90°	0.95	0.87	0.93	0.79	0.96	0.83
Polyphenylene oxide				0.97		1.48
Formvar	0.98	0.86	1.07	0.81	0.98	0.87
Butvar	0.97	0.85	1.02	0.80	1.06	0.84
Nylon 6 - dried		0.92		0.78		0.80
- 1.21% H_2O	0.96	0.88	0.93	0.75	0.88	0.73
- 10.29% H_2O		0.90		0.84		0.83
Nylon 66 - 0.56% H_2O	0.96	0.86	1.33	0.85	1.14	1.05
EPDM rubber:	1.90	1.69	2.12	1.66	1.37	1.21
Ionomer Surlyn	1.13	1.05	1.22	0.93	1.10	0.88
TPR-1900	1.00	0.95	0.99	0.78	0.89	0.74
Kraton-1101	2.92	< 2.82	3.68	2.61	< 2.34	< 1.69
Hytrel 4055	< 1.90	0.64	0.71	0.99	0.57	0.43
Hytrel 6355	0.93	0.88	0.97	0.77	0.89	0.80
SAN + 20% Glass	1.53	1.42	2.14	1.40	1.91	1.20
PP + 20% Glass	1.12	1.04	1.33	1.08	1.29	1.03
PTMT + 20% Glass	1.42	1.19	1.86	1.32	1.65	1.03
PE + 40% Glass	1.28	1.11	1.51	1.02	1.37	0.99
Nylon 66 + minerals	1.21	1.10	1.82	1.18	1.21	0.92
Nylon 66 + 33% Glass (Dry)	1.30	1.16	1.68	1.15	1.49	0.97
- Wet (3.03% Water)		1.11		1.07		0.96